Boundary Dynamics of the XY-Chain with the Density Matrix Renormalization Group

von

Tobias Hövelborn

Diplomarbeit in Physik

angefertigt im

Institut für Theoretische Physik
der Universität zu Köln

vorgelegt der
Mathematisch-Naturwissenschaftlichen Fakultät
der
Rheinischen Friedrich-Wilhelms-Universität
Bonn

Oktober 2000

Ich versichere, daß ich diese Arbeit selbständig verfaßt und keine anderen als die angegebenen Quellen und Hilfsmittel benutzt sowie die Zitate kenntlich gemacht habe.

Bonn, den 17.10.2000

Referent:	Priv.-Doz. Dr. G. S. Uhrig (Universität Köln)
Koreferent:	Prof. Dr. H. Monien (Universität Bonn)

Contents

1 Introduction

The study of physical properties of metallic systems, containing a small fraction of magnetic impurities with internal degrees of freedom, is of general theoretical interest and is essential to explain a lot of experimental features. The fermionic single impurity models are standard examples for strongly correlated electron systems. The minimum of electrical resistivity in some metals, for example in *Au*, at a few Kelvin was one of the puzzles that could be solved by the consideration of 3*d* transition metal impurities, such as *Fe*. J. Kondo showed this in 1964 [1]. Another important contribution to the field was the work of Anderson [2]. The physics of heavy fermions that can be described by the periodic Anderson model, is a challenge for theory and experiment for over twenty years. Although the Anderson model is a rather simplified description of impurities in metallic systems, it failed to yield an exact solution. A thorough review of the Kondo problem and the Anderson model is given by A. C. Hewson in reference [3].

The interest in single impurity models has been revitalised by the systematic mapping of lattice models onto effective single impurity models. This mapping is done in the framework of dynamical mean-field theory (DMFT), which is exact in the limit of infinite coordination number, corresponding to the limit of infinite dimensions $\mathrm{d} \to \infty$, provided that the limit is approached in a suitable manner [4]. This mapping leads to an effective single site problem, resulting in a neglect of spatial fluctuations, but taking the fluctuations in time into account [5–7]. As described in [8, 9], the connection between the lattice problem and the single impurity problem is provided in form of a self-consistency condition for the effective medium, in which the impurity is embedded. The local propagators for lattice problem and impurity problem have to coincide.

A method to obtain accurate results for the spectral density of local propagators of single impurity models should be very useful in an iterative self-consistent approach to $\mathrm{d} = \infty$ lattice problems.

The Anderson model and the Kondo model of single impurities, can be mapped onto linear infinite or semi-infinite fermionic chain Hamiltonians [3]. One can even go further and map these fermionic chains with a Jordan-Wigner transformation [10] on pure spin chains.

Since exact solutions for quantum lattice models are rare one is restricted to approximate analytical methods like perturbation theory or mean field theory, or one tries to apply numerical methods. An approximate analytical approach often fails to describe the essential physics, due to the necessary assumptions

and simplifications. This is especially true in the case of low dimensions.

The exact diagonalization methods are limited to relatively small system sizes. Even for highly symmetric problems one is usually restricted to typically 30 sites or perhaps 36 sites. Since finite size effects can be very strong, and since we are interested in large systems or even in the thermodynamic limit, exact diagonalization is not feasible. Also Monte Carlo simulations do not yield results of the desired accuracy.

As a different approach Wilson developed the real-space numerical renormalization group [11], substantially enhanced by White to the density-matrix renormalization group (DMRG) [12]. This method has proved to be very useful in the study of low dimensional quantum systems. The various extensions and improvements to DMRG are reviewed in reference [13].

In this thesis we will give an introduction to single impurity quantum models and their mapping on linear chains. A few analytic results for finite and infinite uniform XY-chains will be derived. These results will serve as a benchmark for the DMRG accuracy. An introduction to DMRG is given and the methods to obtain dynamic properties are reviewed. In this framework we will discuss some ideas for a new correction vector method. Subsequently the DMRG results for static and dynamic properties are presented. This thesis ends with a conclusion, an outlook and suggestions on a possible continuation of the research.

2 Quantum Impurity Models

Subsequently a description of a general quantum impurity Hamiltonian is given, followed by a motivated reduction to the fundamental Anderson and Kondo Hamiltonians. The mapping of these models onto semi-infinite fermionic chains is pointed out, as well as the transformation on spin chains via the Jordan-Wigner transformation. Some exact results for finite and infinite XY-chains will be derived.

2.1 Anderson Model and Kondo Model

An impurity in a metallic host can be described by a very general Hamiltonian [3] that specifies all the particles and their interactions. For N_0 electrons one can write it down in the following form,

$$H = \sum_{i=1}^{N_0} \left(\frac{\mathbf{p}_i^2}{2m} + U(\mathbf{r}_i) + V_{\mathrm{imp}}(\mathbf{r}_i) \right) + \frac{1}{2} \sum_{i \neq j} \frac{e^2}{|\mathbf{r}_i - \mathbf{r}_j|} + \sum_{i=1}^{N_0} \lambda(\mathbf{r}_i) \mathbf{l}_i \cdot \sigma_i \ . \tag{2.1}$$

The first term describes the kinetic energy of the electrons and U represents the periodic potential due to the nuclei of the host metal. V_{imp} specifies the change of the potential caused by the substitution of a host nucleus by an impurity nucleus. The fourth term contributes the coulomb interaction between the electrons and the last term is a relativistic correction due to spin-orbit interaction.

The Hamiltonian looks quite simple but the strong Coulomb interactions prohibit perturbative treatment. The only possible approach is via some kind of self-consistent field theory. In such an approach it is very difficult to obtain accurate results and predictions, especially if we are interested in excitations as well. Instead of examining the full Hamiltonian (2.1) one can construct simpler model Hamiltonians, which describe the low energy excitations associated with the impurity and ignore features that are not direct related to impurity effects.

In these models it is usually assumed, that the host metal has got very broad conduction bands, such as those derived from *s* and *p* states. The electrons in these bands are assumed to behave like independent particles in a periodic potential. These electrons can be treated as quasi-particles, where the quasi-particle interactions are usually neglected due to the predominant delocalization in the broad conduction bands. The host metal conduction electrons can therefore be

described approximately by a one electron Hamiltonian in second quantization,

$$H = \sum_{\mathbf{k},\sigma} \epsilon_{\mathbf{k}} c^{\dagger}_{\mathbf{k},\sigma} c_{\mathbf{k},\sigma} \ , \tag{2.2}$$

where $c^{\dagger}_{\mathbf{k},\sigma}$ and $c_{\mathbf{k},\sigma}$ are creation and annihilation operator, for the Bloch states with wavevector $\mathbf{k}$, energy $\epsilon_{\mathbf{k}}$ and spin σ. The creation and annihilation operators obey the standard anticommutation relations for fermions. The density of states $\rho_0(\epsilon)$ for these conduction electron Bloch waves is assumed to be characterized by a set of Dirac delta functions

$$\rho_0(\epsilon) = \sum_{\mathbf{k}} \delta(\epsilon - \epsilon_{\mathbf{k}}) \ . \tag{2.3}$$

One could attempt to remain in the picture of independent particles for the conduction electrons and extend it by an effective potential $V_{\text{imp}}(\mathbf{r})$. As stated in [3] this approach is not sufficient to describe the interesting features of transition metal or rare earth impurities, but it is quoted here as an intermediate step on the way from (2.2) to the more advanced quantum impurity models. It is useful to express the potential in terms of the Bloch states of the conduction electrons in the pure host metal. Using the coefficients $V_{\mathbf{k},\mathbf{k}'} = \langle \mathbf{k} | V_{\text{imp}} | \mathbf{k}' \rangle$ leads to the simple Hamiltonian

$$H = \sum_{\mathbf{k},\sigma} \epsilon_{\mathbf{k}} c^{\dagger}_{\mathbf{k},\sigma} c_{\mathbf{k},\sigma} + \sum_{\mathbf{k},\mathbf{k}',\sigma} V_{\mathbf{k},\mathbf{k}'} c^{\dagger}_{\mathbf{k},\sigma} c_{\mathbf{k}',\sigma} \ . \tag{2.4}$$

An impurity can also induce a narrow peak in the conduction band known as virtual bound state resonance. If the potential V_{imp} is attractive it may either form a bound state below the conduction band or it may be to weak to exhibit a bound state, but at least V_{imp} may tend to localize the conduction electrons in the vicinity of the impurity. In this case the electrons spend a relatively long time in the impurity region, but wave functions become Bloch states far from the impurity. Hence there is no bound state. This effect can be understood as resonant scattering at the impurity.

Virtual bound state resonances occur for transition metal or rare earth impurities when the *d* or *f* level lies in the conduction band of the host metal. There is an additional effective potential term in the radial Schrödinger equation due to angular momentum, which reads $l(l+1)/r^2$ and tends to localize states with higher angular momentum in a potential barrier. There will be a finite tunneling probability so that these states will be virtual bound states.

Anderson [2] calculated the modification of the atomic *d* functions of the isolated impurity ion due to the embedding in the lattice of metal ions. Introducing the overlap or hybridization matrix element

$$V_{\mathbf{k}} = \sum_{\delta} e^{i\mathbf{k}\mathbf{d}_\delta} \langle \Phi_d | H | \psi_{\mathbf{d}_\delta} \rangle \ , \tag{2.5}$$

where Φ_d is the atomic *d* orbital of the impurity ion and $\psi_{\mathbf{d}_\delta}$ is the Wannier wavefunction of the conduction electrons at the site $\mathbf{d}_\delta$ and H is the full Hamiltonian (2.1). With the *d* level energy of the impurity ϵ_d and the annihilation and creation operators for this state $c_{d,\sigma}$ and $c^\dagger_{d,\sigma}$, the Hamiltonian reads

$$H = \sum_{\sigma} \epsilon_d c^\dagger_{d,\sigma} c_{d,\sigma} + \sum_{\mathbf{k},\sigma} \epsilon_{\mathbf{k}} c^\dagger_{\mathbf{k},\sigma} c_{\mathbf{k},\sigma} + \sum_{\mathbf{k},\sigma} (V_{\mathbf{k}} c^\dagger_{d,\sigma} c_{\mathbf{k},\sigma} + V^*_{\mathbf{k}} c^\dagger_{\mathbf{k},\sigma} c_{d,\sigma}) \ . \tag{2.6}$$

This model Hamiltonian is usually referred to as non-interacting Anderson model. The interaction that is taken into account in the interacting Anderson model is the coulomb repulsion between the electrons in the impurity ion *d* states. Its strength is given by

$$U = \int \Phi^*_d(\mathbf{r}) \Phi^*_d(\mathbf{r}') \frac{e^2}{|\mathbf{r} - \mathbf{r}'|} \Phi_d(\mathbf{r}) \Phi_d(\mathbf{r}') d\mathbf{r} d\mathbf{r}' \ . \tag{2.7}$$

If no or one electron is in the *d* level there is no coulomb repulsion at all. But if two electrons are in the *d* level they repel each other and the energy U due to coulomb potential has to be added to the Hamiltonian. The empty *d* level contributes no energy, $E_{imp}(0) = 0$. One electron contributes the *d* level energy, $E_{imp}(\uparrow) = E_{imp}(\downarrow) = \epsilon_d$. Two electrons add their binding energy and the coulomb repulsion energy, $E_{imp}(\uparrow\downarrow) = 2\epsilon_d + U$.

This interaction can be included in the Hamiltonian of the non-interacting Anderson impurity model in an elegant manner using the particle number operator for the impurity ion, which is defined as $n_{d\sigma} = c^\dagger_{d\sigma} c_{d\sigma}$. The Hamiltonian for the interacting or $(U \neq 0)$ Anderson model reads

$$\begin{aligned} H = \sum_{\sigma} \epsilon_d n_{d,\sigma} + U n_{d,\downarrow} n_{d,\uparrow} + \sum_{\mathbf{k},\sigma} \epsilon_{\mathbf{k}} c^\dagger_{\mathbf{k},\sigma} c_{\mathbf{k},\sigma} \\ + \sum_{\mathbf{k},\sigma} (V_{\mathbf{k}} c^\dagger_{d,\sigma} c_{\mathbf{k},\sigma} + V^*_{\mathbf{k}} c^\dagger_{\mathbf{k},\sigma} c_{d,\sigma}) \ . \end{aligned} \tag{2.8}$$

For the case of vanishing $V_{\mathbf{k}}$ we obtain a simple model that can be solved easily, because the *d* states are not coupled to the conduction electrons at all. In this

simple model we observe a local magnetic moment associated with the two fold degenerate state with single occupation and spin $\frac{1}{2}$. The states with no or two electrons do not form localized magnetic moments. The parameter regime for a local magnetic moment in this simplified model can be derived directly. A criterion for the occupation of the impurity ion *d* state is, that the Fermi energy ϵ_F is higher than the energy of the *d* level. But the Fermi energy must be below the energy of a second electron to prohibit double occupation. Hence the criterion for a local magnetic moment is $\epsilon_d < \epsilon_F < \epsilon_d + U$.

A different approach in the description of magnetic effects is to describe the host metal as a magnetic insulator, and then take the effects of the impurities local magnetic moment on the conduction electrons into account. A model that describes this interaction via a Heisenberg exchange interaction that couples the local moment to conduction electrons with a coupling constant $V_{\mathbf{k},\mathbf{k}'}$ is the *s-d* model, which is often referred to as the Kondo model

$$\begin{aligned} H_{sd} &= \sum_{\mathbf{k},\sigma} \epsilon_{\mathbf{k}} c^{\dagger}_{\mathbf{k},\sigma} c_{\mathbf{k},\sigma} + \\ &\sum_{\mathbf{k},\mathbf{k}'} J_{\mathbf{k},\mathbf{k}'} (S^{+} c^{\dagger}_{\mathbf{k}\downarrow} c_{\mathbf{k}\uparrow} + S^{-} c^{\dagger}_{\mathbf{k}\uparrow} c_{\mathbf{k}\downarrow} + S^{z} (c^{\dagger}_{\mathbf{k}\uparrow} c_{\mathbf{k}\uparrow} - c^{\dagger}_{\mathbf{k}\downarrow} c_{\mathbf{k}\downarrow})) \ . \end{aligned} \quad (2.9)$$

Kondo used this Hamiltonian to explain the minimum total resistivity [1].

Schrieffer and Wolff [14] showed that the Anderson Hamiltonian (2.8) in the local magnetic moment regime, characterized by single occupation in the impurity *d* level, is equivalent to an effective *s-d* Hamiltonian. The parameter regime of the local magnetic moment for the Anderson model includes the range $\epsilon_d \ll \epsilon_F \ll \epsilon_d + U$ with $|\epsilon_d + U - \epsilon_F|, |\epsilon_F - \epsilon_d| \gg \Delta$, where Δ is the width of the virtual bound state resonance. More precise criteria for a local moment are derived in [3], for example.

If one of the criteria $|\epsilon_d + U - \epsilon_F|, |\epsilon_F - \epsilon_d| \gg \Delta$ fails, that is if one of the levels $\epsilon_d + U$ or ϵ_d approaches the Fermi level, the Schrieffer-Wolf transformation to the *s-d* model breaks down. The impurity occupation number fluctuates between two different values. This regimes are called mixed or intermediate valence regimes. They are of interest for the description of certain rare earth compounds, for example SmB_6. The number of *f* electrons at the *Sm* ions is not integral. The ionic state is a dynamic mixture of Sm^{2+} and Sm^{3+}.

There are two parameter regimes that show no local magnetic moment. One is the empty orbital regime, which is characterized by an impurity state where the occupation number is zero. The criterion for this regime is $\epsilon_d - \epsilon_F \gg \Delta$. In this case the Fermi level is clear below the *d* level. Hence the *d* level is unoccupied.

The other regime is $\epsilon_d + U - \epsilon_F \ll \Delta$. In this case the high Fermi energy guarantees double occupancy of the *d* level. The regimes without a local magnetic moment are probably of least interest, but they are rather easy to describe due to negligible charge fluctuations and a non-degenerate ground state [3].

2.2 Mapping onto a Linear Chain

If we assume that the interaction in (2.9) is separable in a sense that it can be written as $J_{\mathbf{k},\mathbf{k}'} = \alpha_k \alpha_{k'} J$, the exchange interaction between the localized spin S and the spin of a localized one electron state with a creation operator $c^\dagger_{0,\sigma}$ reads

$$c^\dagger_{0,\sigma} = \sum_{\mathbf{k}} \alpha_k c^\dagger_{\mathbf{k},\sigma} \ , \tag{2.10}$$

with α_k chosen according to $\sum_{\mathbf{k}} |\alpha_k|^2 = 1$. The spin interaction part of the *s-d* Hamiltonian (2.9) can be rewritten as

$$H_{sd,spin} = 2J\mathbf{S} \cdot c^\dagger_{0,\sigma}(\mathbf{s}_0)_{\sigma,\sigma'} c^\dagger_{0,\sigma'} \ , \tag{2.11}$$

where $\mathbf{s}_0$ is the spin of the localized one electron state.

Following the derivation in [3], we can construct a new basis using the Lanczos algorithm to tridiagonalize the conduction electron part of the *s-d* Hamiltonian denoted as H_c. Starting from the localized single electron state $|0\rangle$ we can obtain the basis from the sequence $|0\rangle, H_c|0\rangle, H_c^2|0\rangle, H_c^3|0\rangle \ldots$ by Schmidt orthogonalization and normalization.

If we denote the n-th state of the basis by $|n\rangle$, the Lanczos recursion relations are

$$|n+1\rangle = \frac{1}{\gamma_n}\left(H_c|n\rangle - |n\rangle\langle n|H_c|n\rangle - |n-1\rangle\langle n-1|H_c|n\rangle\right) \ , \tag{2.12}$$

resulting in a basis that tridiagonalizes H_c. Multiplying (2.12) on the left by $\langle m|$ we see, that $\langle m|H_c|n\rangle$ vanishes, except for the cases

$$\begin{aligned} \langle n-1|H_c|n\rangle &= \gamma^*_{n-1} \\ \langle n|H_c|n\rangle &= \epsilon_n \\ \langle n+1|H_c|n\rangle &= \gamma_n \ , \end{aligned} \tag{2.13}$$

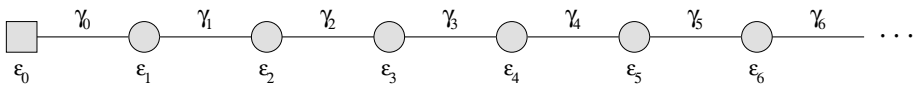

Figure 1: Semi-infinite chain with impurity as boundary site.

where the label ϵ_n is implicitly defined by this equation. We can write down the action of the Hamiltonian on a state $|n\rangle$ as

$$H_c|n\rangle = \gamma_n|n+1\rangle + \epsilon_n|n\rangle + \gamma_{n-1}^*|n-1\rangle \ . \tag{2.14}$$

The Hamiltonian can therefore be rewritten with creation and annihilation operators for the new basis states

$$H_c = \sum_{n,\sigma} \epsilon_n c_{n,\sigma}^\dagger c_{n,\sigma} + \sum_{n,\sigma} (\gamma_n c_{n,\sigma}^\dagger c_{n+1,\sigma} + \gamma_n^* c_{n+1,\sigma}^\dagger c_{n,\sigma}) \ . \tag{2.15}$$

Tridiagonalizing the primarily diagonal operator H_c seems to be no big achievement, but if we combine the conduction electron part H_c in the new basis with the impurity spin interaction part, we yield the entire *s-d* model in form of a semi-infinite tight-binding linear chain. The impurity is localized at the end of the chain as shown schematically in Fig. 1. The basis states of the conduction electrons have been chosen in such a manner that the impurity couples directly to a local orbital, that in turn couples directly to the Bloch states of conduction electrons.

The same technique can be applied to the Anderson model (2.8). Again the combination of states which is directly coupled to the impurity is mapped onto the first site of the chain,

$$c_{0,\sigma}^\dagger = \frac{1}{V} \sum_{\mathbf{k}} V_{\mathbf{k}} c_{\mathbf{k}}^\dagger . \tag{2.16}$$

Using a Lanczos recursion (2.12) in the same manner as in the *s-d* case we obtain a semi-infinite chain Hamiltonian that is equivalent to the Anderson Hamiltonian (2.8). For a more detailed discussion see [3], for example. The linear chain version of the Anderson model reads

$$\begin{aligned} H = &\sum_{\sigma} \epsilon_d n_{d,\sigma} + U n_{d,\downarrow} n_{d,\uparrow} + \sum_{\sigma} (V c_{d,\sigma}^\dagger c_{0,\sigma} + V^* c_{0,\sigma}^\dagger c_{d,\sigma}) \\ &+ \sum_{n,\sigma} \gamma_n (c_{n,\sigma}^\dagger c_{n+1,\sigma} + c_{n+1,\sigma}^\dagger c_{n,\sigma}) + \sum_{n,\sigma} \epsilon_n c_{n,\sigma}^\dagger c_{n,\sigma} \ , \end{aligned} \tag{2.17}$$

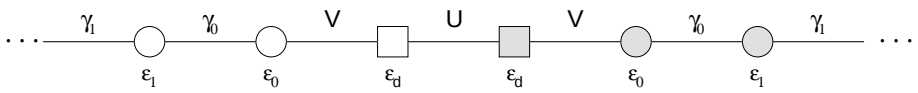

Figure 2: Infinite spin chain as equivalent version of the periodic single impurity Anderson model. Each half chain corresponds to a fixed spin direction.

where ϵ_n and γ_n are calculated via the tridiagonalization procedure. Hence they are functions of $\epsilon_{\mathbf{k}}$ and $V_{\mathbf{k}}$.

The linear chain versions of the single impurity models are rather useful when it comes to the point of computational calculations. Each of the fermionic sites in these impurity chains has got four degrees of freedom. It simplifies the structure of the involved computer algorithms even more, if we project the fermionic degrees of freedom onto spin degrees of freedom. This is done by the so called Jordan-Wigner transformation [10]. The basic idea is to identify spinless fermion operators with spin $\frac{1}{2}$ operators in the following manner

$$\begin{aligned} c_n &\Rightarrow e^{i\pi\sum_{j=1}^{n-1} S^+(j)S^-(j)} S^-(n) \\ c_n^\dagger &\Rightarrow S^+(n) e^{-i\pi\sum_{j=1}^{n-1} S^+(j)S^-(j)} . \end{aligned} \tag{2.18}$$

The inverse transformation reads

$$\begin{aligned} S^-(n) &\Rightarrow e^{i\pi\sum_{j=1}^{n-1} c_n^\dagger c_n} c_n \\ S^+(n) &\Rightarrow c_n^\dagger e^{-i\pi\sum_{j=1}^{n-1} c_n^\dagger c_n} . \end{aligned} \tag{2.19}$$

By substituting $c_n^\dagger c_n$ and $c_n c_n^\dagger$ with the expressions in (2.18) and using the fact that the spin operators for different sites commute it is straight forward to obtain the following relations

$$\begin{aligned} c_n^\dagger c_n &= S^+(n)S^-(n) &&= \frac{1}{2} + S^z(n) \\ c_n c_n^\dagger &= S^-(n)S^+(n) &&= \frac{1}{2} - S^z(n) . \end{aligned} \tag{2.20}$$

Applying these transformations, the linear chain version of the single impurity Anderson model (2.17) can be mapped onto an infinite spin $\frac{1}{2}$ chain as in Fig. 2. The two impurity states are mapped onto two sites and each of them is connected to a semi-infinite chain. The infinite chain spin Hamiltonian is constructed reflection symmetric with respect to the impurity sites. Each semi-infinite chain

represents one spin direction. For example one could map all the up spins onto the left half chain and all the down spins onto the right half chain. The repulsive Coulomb interaction is realized via an $US_i^zS_{i+1}^z$ type interaction between the impurity sites in the middle. The conduction electron sites are connected via terms of S^+S^- type.

2.3 Homogeneous Spin $\frac{1}{2}$ XY Model

The Anderson impurity model can be mapped on a spin $\frac{1}{2}$ chain. We are going to examine, how accurate local dynamical correlation functions can be calculated with the means of the density-matrix renormalization approach. In order to make finite size effects and errors due to the method distinguishable, the very simple and directly solvable homogeneous spin $\frac{1}{2}$ XY-model on a semi-infinite chain will be examined, instead of the single impurity Anderson model. The Hamiltonian reads

$$H_{XY}^{\infty} = \sum_{n=1}^{\infty} t\left(S^+(n)S^-(n+1) + S^-(n)S^+(n+1)\right) \ . \tag{2.21}$$

This Hamiltonian can be transformed into a chain of spinless fermions using the Jordan-Wigner relation (2.18)

$$H_{XY}^{\infty} = \sum_{n=1}^{\infty} t\left(a_n^\dagger a_{n+1} + a_n a_{n+1}^\dagger\right) \ . \tag{2.22}$$

The constant hopping term t will be chosen to be $\frac{1}{2}$ from now on.

One can can calculate the exact ground state energy by examining a finite chain of L sites in the fermionic picture. We use open boundary conditions to consider, that the left site will become a boundary site when we approach (2.22), i. e. the thermodynamic limit. The Hamiltonian of the finite chain can be written as

$$H_{XY}^{L} = \frac{1}{2}\sum_{n=1}^{L-1}(a_n^\dagger a_{n+1} + a_n a_{n+1}^\dagger) \ . \tag{2.23}$$

The creation operator of a Bloch state with wavevector k for the Hamiltonian above reads

$$c_k^\dagger = \frac{1}{\sqrt{N_k}}\sum_{n=1}^{L} a_n^\dagger \sin nk \ , \tag{2.24}$$

with $k(L+1) = m \cdot \pi$ and $m = 1, \ldots, L$. The restrictions to k result from the fact, that there is no particle creation at the sites with indices 0 and $L+1$. This transformation in $\mathbf{k}$-space is equivalent to a discrete Fourier transformation, taking spatial symmetry and boundary conditions into account.

To obtain the dispersion relation one can calculate the commutator of the Hamiltonian H_{XY}^L and the creator of a Bloch state $c_k^\dagger$. Since the Hamiltonian conserves the particle number, the commutator $H_{XY}^L c_k^\dagger - c_k^\dagger H_{XY}^L$ creates a quasi-particle with wavevector $\mathbf{k}$ multiplied by the change in energy caused by this quasi-particle. In our case, keeping the commutation relations for the a_n in mind, we gain

$$\begin{aligned}
\left[H_{XY}^L, c_k^\dagger\right] &= H_{XY}^L c_k^\dagger - c_k^\dagger H_{XY}^L \\
&= -\frac{1}{2\sqrt{N_k}} \sum_{n=2}^{L-1} \left(a_{n+1}^\dagger + a_{n-1}^\dagger\right) \sin nk \\
&\quad -\frac{1}{2\sqrt{N_k}} a_2^\dagger \sin k - \frac{1}{2\sqrt{N_k}} a_{L-1}^\dagger \sin Lk \\
&= -\frac{1}{2\sqrt{N_k}} \sum_{n=1}^{L} a_n^\dagger \left(\sin\left(n-1\right)k + \sin\left(n+1\right)k\right) \\
&= -\cos k \cdot \frac{1}{\sqrt{N_k}} \sum_{n=1}^{L} a_n^\dagger \sin nk \\
&= -\cos k \cdot c_k^\dagger \,. \qquad (2.25)
\end{aligned}$$

The transformation from third to fourth line is performed via the trigonometric rule $\sin x + \sin y = 2 \sin \frac{x+y}{2} \cos \frac{x-y}{2}$.

The dispersion relation and the restrictions for k given above, yield the energy eigenvalues of the finite XY-chain

$$E_m^L = -\cos \frac{m\pi}{L+1} \text{ with } m \in \{1, 2, \ldots, L\} \,. \qquad (2.26)$$

For $m < \frac{L}{2}$ the energy eigenvalues are negative, for $m > \frac{L}{2}$ positive. To obtain

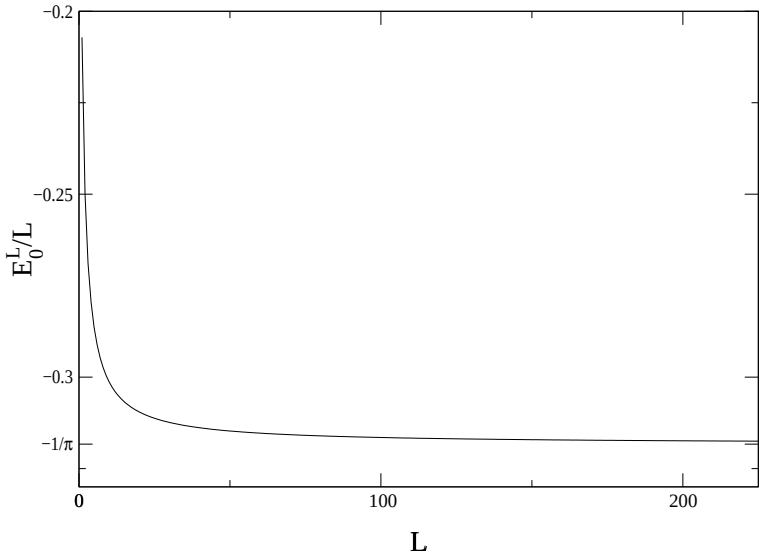

Figure 3: Ground state energy per site for a homogeneous XY-chain with L sites.

the ground state energy we sum up all the negative energy eigenvalues

$$\begin{aligned}
E_0^L &= -\sum_{m=1}^{L/2} \cos\frac{m\pi}{L+1} \\
&= -\frac{1}{2}\sum_{m=1}^{L/2}\left(e^{\frac{im\pi}{L+1}} + e^{-\frac{im\pi}{L+1}}\right) \\
&= -\frac{1}{2}\left(e^{\frac{i\pi}{L+1}}\frac{e^{\frac{i\pi}{L+1}(\frac{L}{2})}-1}{e^{\frac{i\pi}{L+1}}-1} + e^{-\frac{i\pi}{L+1}}\frac{e^{-\frac{i\pi}{L+1}(\frac{L}{2})}-1}{e^{-\frac{i\pi}{L+1}}-1}\right) \\
&= -\frac{1}{2}\left(\frac{e^{\frac{i\pi}{L+1}(\frac{L}{2}+1)} - e^{-\frac{i\pi}{L+1}(\frac{L}{2})} - e^{\frac{i\pi}{L+1}} + 1}{e^{\frac{i\pi}{L+1}}-1}\right) \\
&= \frac{1}{2}\left(1 - \frac{e^{\frac{i\pi}{L+1}(\frac{L+1}{2})} - e^{-\frac{i\pi}{L+1}(\frac{L+1}{2})}}{e^{\frac{i\pi}{2L+2}} - e^{-\frac{i\pi}{2L+2}}}\right) \\
&= \frac{1}{2}\left(1 - \frac{\sin\frac{\pi}{2}}{\sin\frac{\pi}{2L+2}}\right) \quad . \qquad (2.27)
\end{aligned}$$

Hence the total ground state energy for an homogeneous XY-chain with L sites

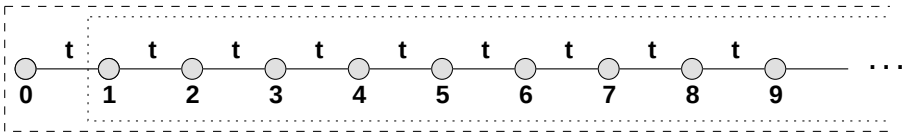

Figure 4: Semi-infinite XY-chain with hopping constant t. Dashed line encloses sites contributing to g_0, dotted line those contributing to g_1.

reads

$$E_0^L = \frac{1}{2}\left(1 - \frac{1}{\sin\frac{\pi}{2L+2}}\right) . \tag{2.28}$$

The total ground state energy per site E_0^L for a XY-chain with L sites is plotted in Fig. 3. The curve converges rapidly. The energy per site limit for an infinite chain can be directly derived from (2.28). As n goes to infinity the argument of the sine goes to zero. To calculate the limit, we substitute the sine by its leading term in the series expansion, its argument. This results in the per site energy of a homogeneous XY-chain in the thermodynamic limit

$$e_{XY} = \lim_{L\to\infty}\frac{E_0^L}{L} = \lim_{L\to\infty}\left(\frac{1}{2L} - \frac{1}{2L\frac{\pi}{2L+2}}\right) = -\frac{1}{\pi} . \tag{2.29}$$

The exact results (2.28) and (2.29) are a good benchmark for the numerical DMRG algorithms, which will be described below.

Hence we are interested in local dynamic properties, we will derive the full local propagator for the boundary spin of a semi-infinite homogenous XY-chain, as given by (2.21) respectively (2.22). A convenient way to obtain the desired result is a perturbative approach in diagrammatic notation. The chain we are going to examine is schematically depicted in Fig. 4.

We want to calculate the Green's function g_0, i.e. the full propagator for the site at the very edge of the chain indexed 0.

If we consider a perturbative approach choosing t as parameter and start with $t = 0$, the propagator is trivial

$$g_0^{(0)}(\omega) = \frac{1}{\omega} . \tag{2.30}$$

The propagator $g_0^{(0)}$ will be symbolized by two crosses, indexed zero and connected by a thin line.

The full propagator g_0 for $t \neq 0$ is represented by a similar symbol, but the connecting line is drawn thickly.

The full propagator for the boundary site of the chain beginning with site one and being semi-infinite will be represented by two crosses indexed with the number one and connected by a thick line. The chain sites that contribute to g_0 and g_1 are shown in Fig. 4. The hopping terms will be symbolized by squares. Each of the squares contributes a factor t to the propagator.

The expansion of the full propagator g_0 in terms of the coupling t between the first two sites in diagrammatic language is shown in Fig. 5.

In lowest order the full propagator g_0 is equal to the propagator $g_0^{(0)}$. In first order a hopping to site one and back is taken into account

$$g_0^{(1)} = g_0^{(0)} + \Sigma g_0^{(0)} = g_0^{(0)} + g_0^{(0)} \cdot g_0^{(0)} \cdot t^2 \cdot g_1 \ , \tag{2.31}$$

with the self energy Σ, which contributes $g_0^{(0)} \cdot t \cdot g_1 \cdot t$ to the propagator.

In second order, as we can see in the diagram Fig. 5 as well, the propagator reads

$$g_0^{(2)} = g_0^{(0)} + \Sigma g_0^{(0)} + \Sigma^2 g_0^{(0)} \ . \tag{2.32}$$

The series expansion of g_0 in t leads to an infinite geometric series. The limit is given by

$$g_0 = \frac{g_0^{(0)}}{1 - \Sigma} \ . \tag{2.33}$$

Substituting $g_0^{(0)}$ by $\frac{1}{\omega}$ and inserting Σ yields

$$g_0 = \frac{1}{\omega - t^2 g_1} \ . \tag{2.34}$$

This equation can be used as a recursion relation to calculate g_0, resulting in a continued fraction. For a homogeneous chain g_0 is equal to g_1, resulting in a self-similarity relation

$$g_0 = \frac{1}{\omega - t^2 g_0} \ , \tag{2.35}$$

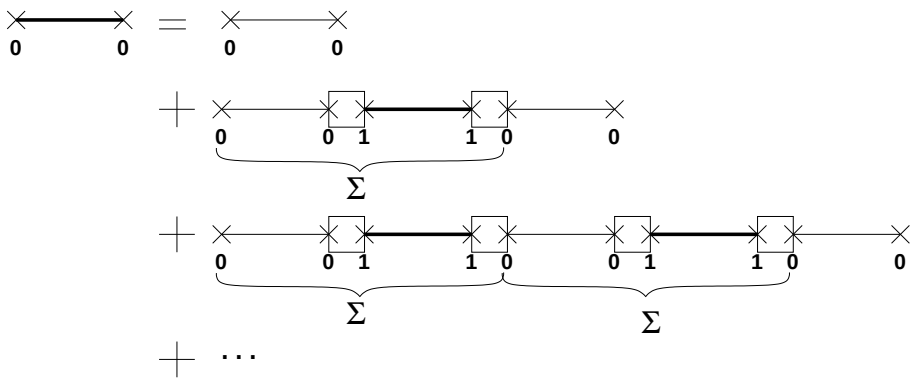

Figure 5: Diagrammatic expansion of the local propagator.

and hence a quadratic equation with the solutions

$$g_0(\omega) = \frac{\omega}{2t^2} \pm \frac{1}{t}\sqrt{\left(\frac{\omega}{2t}\right)^2 - 1}\ ; \quad (t > 0)\ . \tag{2.36}$$

For the hopping parameter $t = \frac{1}{2}$ the solution reads

$$g_0(\omega) = 2\omega \pm 2\sqrt{\omega^2 - 1}\ . \tag{2.37}$$

For $|\omega| \geq 1$ the solution is real. To ensure the that the Green's function decays sufficiently fast for large values of $|\omega|$, i. e. like $1/\omega$, one has to choose the right sign in front of the square root

$$\begin{aligned} g_0(\omega) &= 2\omega + 2\sqrt{\omega^2 - 1}\ ;\ \text{for}\ \omega < -1 \\ g_0(\omega) &= 2\omega - 2\sqrt{\omega^2 - 1}\ ;\ \text{for}\ \omega > 1\ . \end{aligned} \tag{2.38}$$

In the interval of interest, i. e. $|\omega| \leq 1$, the Green's function becomes complex. The retarded solution reads

$$g_R(\omega) = 2\omega - 2i\sqrt{1 - \omega^2}\ ;\ \text{for}\ |\omega| < 1\ . \tag{2.39}$$

The real and imaginary parts of the local Green's function are plotted in Fig. 6.

The density of states $\rho(\omega)$ is given by

$$\rho(\omega) = -\frac{1}{\pi}\mathrm{Im}g_R(\omega) = \frac{2}{\pi}\sqrt{1 - \omega^2}\ . \tag{2.40}$$

Hence the density of states takes the shape of a rescaled half circle.

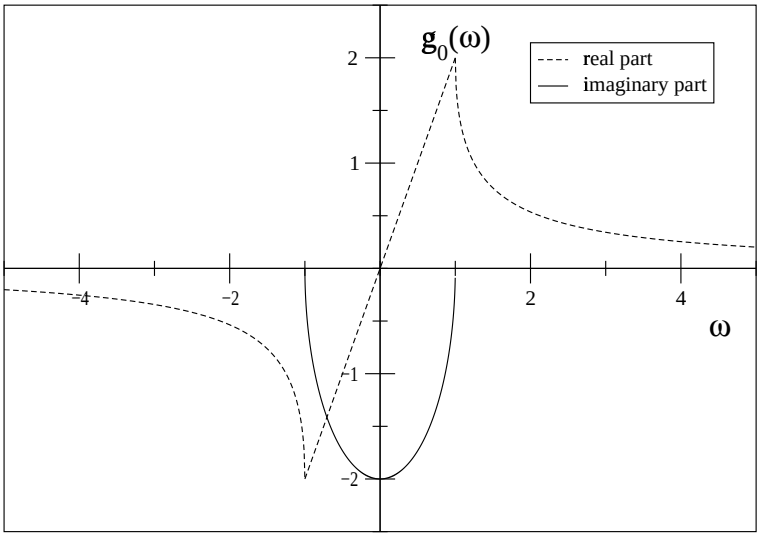

Figure 6: Real and imaginary part of the local Green's function of the semi-infinite XY-chain with hopping term $t = \frac{1}{2}$.

3 Density-Matrix Renormalization Group

The size of the Hilbert space representing a quantum system on a chain grows exponentially with the length of the chain. Therefore it is usually impossible to determine the ground state or other properties of large systems exactly. Hence one is often interested in approximate solutions for very long chains as an estimate for the exact solutions for infinite or semi-infinite chains.

There is a group of methods to gain approximate solutions that is based on a renormalization idea. The basis of these methods is to calculate the desired properties in a reduced Hilbert space.

One method, which is to some extent the precursor of DMRG, is the (real-space) numerical renormalization group technique. This method is based on the idea of dividing the system, for example a spin system, into small blocks, which can be treated separately. When connecting the blocks to describe the entire system, only the few lowest lying eigenstates of each block are taken into account. With this procedure one gains an approximate basis for the entire system, which should be suitable to describe the ground state. Wilson succeeded in solving the single impurity Kondo problem with this method [11]. Subsequently there was a considerable interest in applying this real-space blocking technique to a variety of quantum lattice models, but it turned out to be rather unreliable, even for calculating the ground state energy of a Heisenberg spin chain or the Hubbard model, as discussed in [12, 15].

3.1 Foundation of DMRG

In 1992 Steven R. White introduced the density-matrix version of the numerical renormalization group technique (DMRG). A detailed review of the principles of DMRG is given in [15], and the different extensions and developments are reviewed in [13].

The flaw of the real-space approach is, that it ignores the embedding of the block in the entire system, when it comes to the point of reducing the basis. The choice of the optimal basis depends only on properties of the isolated subsystem, i. e. on its energy eigenvalues. DMRG considers the embedding of the blocks into the entire system.

Which mathematical criterion is suitable to select a reduced Hilbert basis in a way, that the approximate ground state $|\Phi'\rangle$ is still a good representation of the exact ground state $|\Phi\rangle$? This requirement is equivalent to the minimization

of the following term

$$S = ||\Phi\rangle - |\Phi'\rangle|^2 \ . \tag{3.1}$$

The system is divided in two contiguous subsystems with exact and complete sets of basis states $|i\rangle$, respectively $|j\rangle$ with $i = 1, 2, ..., I$, $j = 1, 2, ..., J$ and $I \leq J$. If we consider for example a chain, then cutting the chain into two contiguous sub-chains would be a possible and obvious choice of subsystems. Now we are able to expand the exact state of the entire system in these subsystem states

$$|\Phi\rangle = \sum_{i,j} \Phi_{ij} |i\rangle|j\rangle \ . \tag{3.2}$$

It is useful to express (3.1) in terms of a trace [16]

$$S = \mathrm{tr}\{(\Phi - \Phi')^\dagger (\Phi - \Phi')\} \ . \tag{3.3}$$

The solution of this minimization problem can be obtained via the singular value decomposition (SVD) [17] of the rectangular matrix Φ, i. e.

$$\Phi = UDV^\dagger \ , \tag{3.4}$$

with the unitary $I \times I$ matrix U and the unitary $J \times J$ matrix V. The diagonal $I \times J$ matrix $D = \mathrm{diag}(\sigma_1, ..., \sigma_I)$ contains the singular values. The states of the first subsystem form the columns of U, those of the second subsystem form the columns of V. Due to the unitarity of U and V we can easily express Φ' using the same transformation

$$\Phi = UD'V^\dagger, \ \text{with } D' = U^\dagger \Phi' V \ . \tag{3.5}$$

The truncation error (3.3) reads now

$$\begin{aligned} S &= \mathrm{tr}\{(\Phi - \Phi')^\dagger (\Phi - \Phi')\} && (3.6)\\ &= \mathrm{tr}\{V(D - D')^\dagger U^\dagger U (D - D')V^\dagger\} && (3.7)\\ &= \mathrm{tr}\{(D - D')^\dagger (D - D')\} && (3.8)\\ &= \sum_{ij} |\sigma_i - \sigma'_{i,j}| \ . && (3.9) \end{aligned}$$

The last term shows, that D' has to be chosen in diagonal form, in order to minimize S. In other words, as we are looking for an optimal Φ', the optimal Φ' has got a singular value decomposition with U,V and D'.

To avoid the complicated singular value decomposition, one can have a look at the density-matrix of the system

$$\rho = |\Phi\rangle\langle\Phi| \ . \tag{3.10}$$

Summation over the second subsystem yields the so called reduced density-matrix

$$(\rho_1)_{ii'} = \sum_j \Phi_{ij}\Phi_{i'j} \ , \tag{3.11}$$

or in matrix formulation

$$\rho_1 = \Phi\Phi^\dagger \ . \tag{3.12}$$

Utilizing the singular value decomposition and the fact that V is unitary we get

$$\begin{aligned} \rho_1 &= UDV^\dagger VDU^\dagger \\ &= UD^2U^\dagger \ . \end{aligned} \tag{3.13}$$

The matrix U diagonalizes the reduced density-matrix. The eigenvalues of ρ_1 correspond to the squared elements of the diagonal matrix D and are therefore positive. The columns of U form the eigenvectors of the density-matrix.

From (3.13) we see, that we need not to perform a singular value decomposition, but we can obtain U and D by diagonalizing the reduced density-matrix.

Without any loss of generality we can assume that the eigenvalues are sorted in descending order. A basis truncation should be equivalent to the substitution of D by $D' = \mathrm{diag}(\sigma_1, ..., \sigma_m, 0, 0, 0)$. Only the first m states, i.e. columns of U, are kept. The truncation error (3.6) for this case reads

$$S = \sum_{i=m+1}^{I} \sigma_i^2 \ . \tag{3.14}$$

The squared diagonal elements, corresponding to the discarded columns of U, are a norm of the error that is caused by the basis truncation. This error is minimized indeed, if we keep the eigenstates of the density-matrix belonging to the high eigenvalues and discard those with small eigenvalues.

It can be readily understood, that the choice of these eigenstates of ρ_1 is the optimal one indeed. The reduced density-matrix plays the role of a statistical operator, i.e. the eigenvalues of ρ_1 indicate the statistical weight of the corresponding eigenstate in the representation of $|\Phi\rangle$, if we choose the eigenstates

of the reduced density-matrix as basis states. Since the reduced density-matrix arises from calculating the trace over the $|j\rangle$ states, it contains information about the embedding of the considered subsystem in the entire system. This aspect explains why DMRG is able to overcome the flaws of real-space renormalization group mentioned above.

The DMRG method allows for a systematic truncation of the basis of a subsystem block. By keeping the most probable states it optimizes the approximate representation of a wave function of the entire system. This wave function is named target state below and it is not necessarily the ground state.

The reduced density-matrix can be directly calculated for any state. This includes mixed states. In this case the density-matrix is a superposition of the matrices for the different states $|\phi_k\rangle$. If the probability for the system to be in $|\phi_k\rangle$ is p_k, the reduced density-matrix reads

$$(\rho_1)_{ii'} = \sum_k p_k \sum_j \Phi_{k,ij}\Phi_{k,i'j} \ . \tag{3.15}$$

The algorithmic realizations of this method, which utilize the density-matrix renormalization idea to determine properties of the entire quantum chain system, are described in the next sections.

3.2 Infinite-Size DMRG Algorithm

The simplest version of DMRG is the infinite-size algorithm. As the name suggests this method is intended to describe a quantum chains behavior in the thermodynamic limit $L \to \infty$. The label "infinite-size" is slightly misleading because numerically no systems of infinite length are treated. The method is based on investigating systems of growing size, identifying convergent properties and taking their limits as an approximation for the values at infinite system size. With growing system size growing truncation errors cause rather significant errors, especially in the approximate correlation functions. Higher accuracy can be gained by applying the finite-size algorithm described below.

The infinite-size DMRG algorithm is shown in Tab. 3.2. This algorithm increases the system size in each iteration and the basis is kept at the same size by truncation.

We start from a system block consisting of a quantum chain with a few sites that can be treated exactly. We have to construct and keep track of the

Table 1: The infinite-size DMRG algorithm.

1.	Start with a small initial block A and operators needed to describe interactions of A with the environment.
2.	Build new block $A\bullet$ consisting of A and a single site.
3.	Construct a superblock $B = A\bullet\bullet A'$ consisting of A, the reflection A' of A, and two single sites. Construct the operators for quantities of interest.
4.	Diagonalize the superblock B to find the target state. Measure expectation values of operators if desired.
5.	Form the reduced density-matrix ρ for the block $A\bullet$.
6.	Diagonalize ρ. Keep m eigenstates with largest eigenvalues. Discard the rest.
7.	Replace A by the block $A\bullet$ in the new truncated basis. Transform all operators to the new basis.
8.	Restart from step 2.

operators that are necessary to link the block to another one, as well as those that we need to calculate the Hamiltonian of the entire system. We usually store the Hamiltonian of the block and the operators of the sites at the edges of the block. Furthermore we have to keep track of the operators for the calculation of the expectation values, that we are interested in.

The system block is enlarged by one site and embedded in a large system. The large system consists of the system block ($A\bullet$), whose basis we are going to truncate, and an environment block, which in our case is the reflection of the system block ($\bullet A'$). This choice of the environment block is the obvious one for reflection symmetric chains with open boundary conditions. For asymmetric systems, for example, one would use a small block of a few sites that can be treated exactly and is a good continuation for the chain. The entire system consisting of system block and environment block is sometimes called superblock. In the considerations of section 3.1, $|\Phi\rangle$ always was assumed to be known. The target state (e. g. the ground state) for large systems is usually unknown, and it is the numerically most expensive task in the algorithm to find the ground state (and low lying excited states if desired) of the superblock. If we keep m basis states to describe the system block A, the Hilbert space of the superblock has got the dimension $s^2 \times m^2$, where s is the number of states per site, i. e. $s = 2$ in

the case of $S=1/2$ spin systems.

The next step, after determining the target state, is to calculate the reduced density-matrix and diagonalize it. The m lowest eigenvalues are selected and the corresponding eigenvectors form a rectangular transformation matrix T. All the operators describing the enlarged system block $A\bullet$ can be transformed like

$$\mathrm{H}_{A,\mathrm{new}} = \mathrm{T}\mathrm{H}_{A\bullet}\mathrm{T}^{\dagger} , \tag{3.16}$$

mapping from a basis of dimension $s\times m$ to a basis of dimension m. The new block represents, compared to the one we started with, a system enlarged by one site but with a basis of the same dimension. This block is used to start the next iteration.

3.3 Finite-Size DMRG Algorithm

In the infinite-size DMRG method accuracy for a certain chain length L can only be improved by choosing a larger basis, i. e. a larger m. The finite-size method is a modification that allows for significant improvements in accuracy for a given system size of L without increasing m.

If we stop the infinite-size algorithm at system size L, the operators describing the two sites in the middle are treated exactly, whereas those at the very edge have been transformed rather often. This feature leads to a favouring of states, that depend more on sites in the middle than on sites at the edges.

In each step of the infinite-size algorithm the basis is optimized to represent the target state in a superblock of N sites, but the next step this basis is used to describe a superblock with $N+2$ sites. Hence the basis is never optimized to represent a system of exactly the right size.

This weaknesses of the infinite-size algorithm are overcome by the finite-size method. The finite-size method starts with the infinite-size method up to the desired length L. This time, all operators needed to describe the blocks A are stored in memory for the different block lengths. From know on the environment block is chosen in a way that the superblock length is always equal to L. The left part of the superblock is considered as system block and enlarged until the right part, the environment block, is so small, that it can be treated exactly. The operators associated with the system blocks are stored for all occurring block sizes. These stored blocks are used as environment blocks now. The right part of the superblock is considered as system block and enlarged until the environment block on the left is exact. One can sweep through the system this

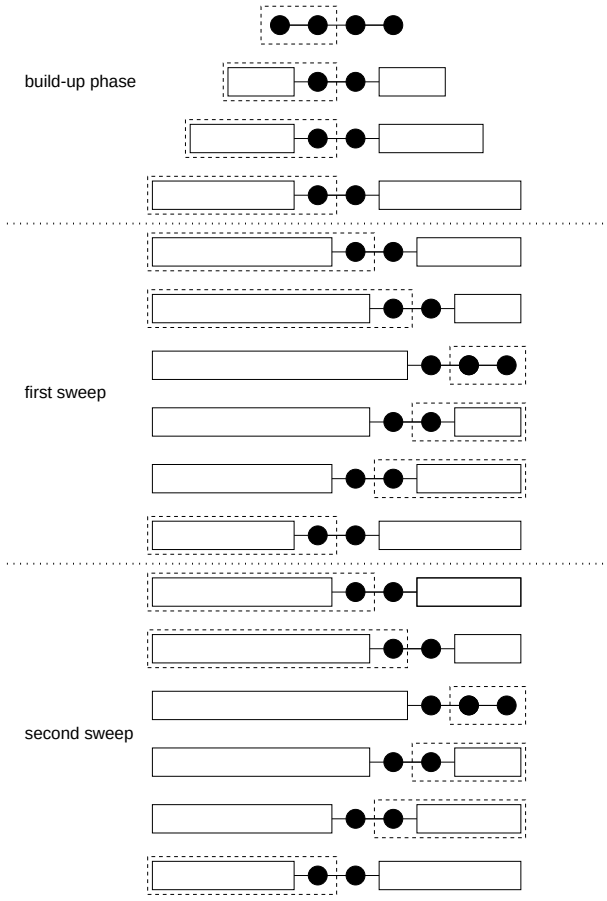

Figure 7: Scheme of the finite size DMRG algorithm for a reflection symmetric system. Build-up phase followed by two sweeps. The basis and operators of the blocks in dashed boxes are calculated at each step.

way several times, always keeping the total length constant and using according environment blocks, that have been stored during the last sweep.

The build-up phase and the sweeps for a symmetric system and for a system without reflection symmetry are shown in the schemes Fig. 7 and Fig. 8. The system blocks are enclosed in boxes in dashed line-style. They consist of a block obtained in the previous step and an additional site. During the sweeps the environment blocks are retrieved from the last, i. e. best, approximation of a block of the desired size. As one can see in Fig. 7 and Fig. 8 the utilization of the reflection symmetry results in a shorter and faster build-up phase. The gain of the symmetry is even more distinct during the sweeps. With reflection symmetry one can continuously sweep from one edge to the middle and back to

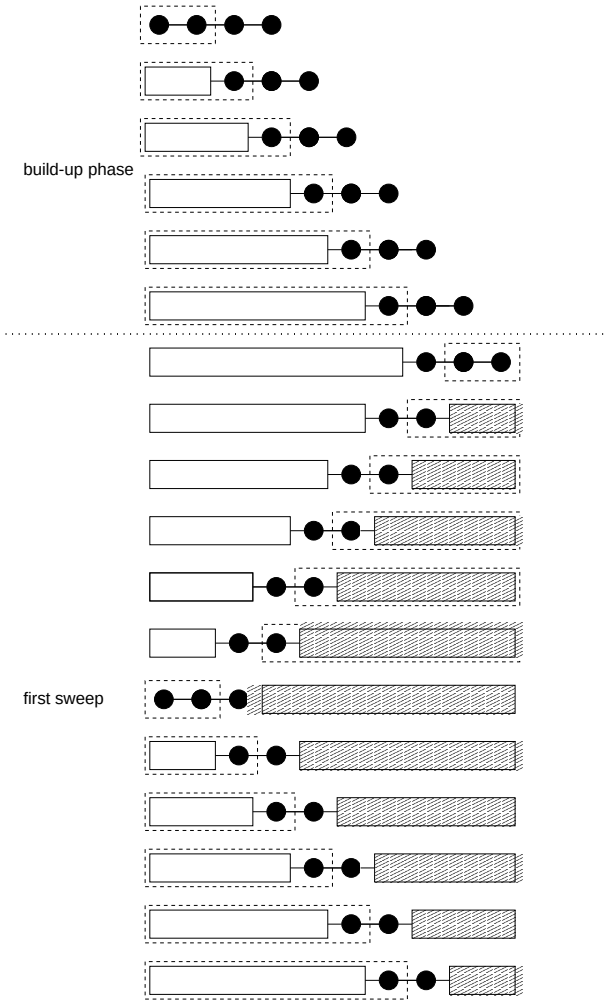

Figure 8: Scheme of the finite size DMRG algorithm for an asymmetric system. Build up phase followed by one sweep.

the same edge, but nevertheless we obtain left and right blocks of all the needed sizes by simple reflection. A sweep for the symmetric problem takes half as long as for a system without reflection symmetry. The storage requirement for all the blocks of different sizes and the corresponding operators of interest is half as large for the symmetric case as for the asymmetric case.

It can be taken as a principle advice to exploit as many symmetries as possible to reduce the computational expense of DMRG. This is especially true for the reflection symmetry, because its consideration doesn't result in a more complicated algorithm but in a gain of time and storage.

3.4 Expectation Values

A great feature of DMRG is to provide the possibility to calculate not only eigenvalues, i. e. energies, but also eigenvectors and thus correlation functions. When calculating correlation functions, you have to consider, whether the operators supplying the expectation values of interest, are lying in the same block of the system or in different ones. This is due to the fact, that the truncated DMRG basis forms no complete set of basis vectors. This leads to additional truncation errors if operators are located in the same system part and one is interested in the expectation value for the product of these. In this case not the single operators, but their product has to be stored and transformed, to avoid the calculation of the matrix product in the incomplete truncated basis. For a detailed discussion see [12, 15].

In the following only local operators will be considered. They are calculated as usual

$$\langle \Phi | A_i | \Phi \rangle \ . \tag{3.17}$$

The expectation values should be calculated, when the finite size sweep is in the middle of the system, i. e. the two constituting blocks are of equal size. In this case the averaged truncation errors are smallest. We didn't do so in every case, because calculating rather fast decaying local correlations on a single site of the system requires higher accuracy in the vicinity of this site. Hence we measure the correlation functions when the block, that contains the site of interest, is smaller, i. e. it is represented with a higher accuracy.

4 Dynamics with DMRG

The DMRG allows calculations of static ground state properties and low-lying energies. There also have been different extension of the basic ideas to allow for the calculation of dynamical properties as well [13]. One method is the Lanczos vector method [18]. In this method DMRG is used optimize the basis of a system to represent Lanczos vectors, which are finally used to calculate the correlation function. The correction vector methods optimize the basis to represent a frequency specific correction vector. A method that obtains the correction vector by matrix inversion will be called inversion method below [19]. A new correction vector scheme that utilizes an energy selective projection operator is described, although it is not yet very sophisticated.

4.1 Dynamical Correlation Functions

The time dependent correlation function at $T = 0$ is given by

$$C_A(t - t') = \langle \psi_0 | A^\dagger(t) A(t') | \psi_0 \rangle \ , \tag{4.1}$$

where $|\psi_0\rangle$ denotes the ground state and $A(t)$ is the Heisenberg representation of A, i. e.

$$A(t) = e^{iH(t)} A e^{-iH(t)} \ . \tag{4.2}$$

The Fourier transform reads

$$C_A(\omega) = \sum_n |\langle \psi_n | A | \psi_0 \rangle|^2 \delta(\omega - (E_n - E_0)), \tag{4.3}$$

where the sum runs over all eigenstates of the Hamiltonian H with the energy E_n. E_0 is the ground state energy. As we are interested in local properties only, i. e. our operators A are not dependent of a wavevector, we don't have to bother about the calculation of operators for a specific wavevector. Kühner and White describe in reference [19] how such operators can be obtained for open boundary conditions.

Expressed in terms of a Green's function the correlation function can be obtained as

$$C_A(\omega) = -\frac{1}{\pi} \lim_{\eta \to 0^+} \mathrm{Im} G_A(\omega + i\eta + E_0) \ . \tag{4.4}$$

The Green's function is defined as

$$G_A(z) = \langle\psi_0|A^\dagger(z-H)^{-1}A|\psi_0\rangle, \tag{4.5}$$

with $z = \omega + i\eta$.

4.2 Lanczos Method

The Lanczos method for DMRG was introduced by K. Hallberg [18]. It is relatively fast and easy to implement but not as accurate as correction vector methods [20].

The Green's function (4.5) can be rewritten in form of a continued fraction

$$G_A(z) = \frac{\langle\psi_0|A^\dagger A|\psi_0\rangle}{z - a_0 - \frac{b_0^2}{z-a_1-\frac{b_1^2}{z-\dots}}}\ , \tag{4.6}$$

where the coefficients a_n and b_n are given by the well known Lanczos recursion relation

$$|f_{n+1}\rangle = H|f_n\rangle - a_n|f_n\rangle - b_{n-1}|f_{n-1}\rangle\ , \tag{4.7}$$

where

$$\begin{aligned} |f_0\rangle &= A|\psi_0\rangle \\ a_n &= \frac{\langle f_n|H|f_n\rangle}{\langle f_n|f_n\rangle} \\ b_{n-1} &= \frac{\langle f_n|f_n\rangle}{\langle f_{n-1}|f_{n-1}\rangle} \text{ and } b_{-1} = 0\ . \end{aligned} \tag{4.8}$$

In the Krylov space, i. e. in the basis of the normalized $|f_n\rangle$, the Hamiltonian takes the following tridiagonal form

$$H = \begin{pmatrix} a_0 & b_0 & & & 0 \\ b_0 & a_1 & b_1 & & \\ & b_1 & a_2 & b_2 & \\ & & \ddots & \ddots & \ddots \\ 0 & & & & \end{pmatrix} \tag{4.9}$$

The Green's function of a finite system has got a finite number of poles. Hence only a finite number of coefficients a_n and b_n appear. DMRG is a good

framework for the calculation of these coefficients. Although the number of coefficients is finite, it is not feasible to calculate all of them. Luckily, the few first ones provide a good approximation to the shape of the Green's function [20]. The ground state, the Hamiltonian H and the operator A are well described in the schemes of the standard DMRG algorithms. To calculate the coefficients with the desired accuracy, it is necessary, that the relevant excited states $|\psi_n\rangle$ are described in good precision, too. This can be achieved by constructing a mixed target state with the dominant weight on the ground state $|\psi_0\rangle$ and the rest of the weight distributed over the first few Lanczos vectors $|f_n\rangle$ with $n = 0, 1, \ldots$ This leads to an inclusion of the relevant excited states, which are connected to the ground state via the operator A, in the reduced Hilbert space.

The number of states kept in the basis m is limited, of course. Hence one has to compromise regarding the decision on how many Lanczos vectors should be included in the target state. If one keeps m basis states and targets on n vectors, the accuracy of each one can be compared to a simple target state with only m/n vectors in the reduced basis. The more vectors are included the less accurate is their representation in the reduced basis.

As stated in [20], the improvement in accuracy by including more than just a few Lanczos vectors into the target state is marginal. One can also address the question on how to assign the weight among the Lanczos states [19, 20]. In the following a small number of Lanczos vectors will be used as target states. These can be represented with the desired accuracy simultaneously, by choosing an equal distribution of weights among the Lanczos vectors.

When calculating the desired spectra, not only those Lanczos vectors are used, that have been used as target states, but the recursion is continued since orthogonality breaks down.

4.3 Correction Vector Methods

The Lanczos vector method allows the calculation of dynamic correlation functions on the entire frequency range. But this gives reason to a weakness of this approach. Usually only the low-energy properties of the correlation functions can be extracted with the desired accuracy. Instead of using the Lanczos vector method, which uses the tridiagonalization of the Hamiltonian to select the important states to be kept, the spectrum can be calculated for a specified frequency. This is done by optimizing the basis to represent a correction vector, that depends on the frequency and on the operator, for which we want to obtain

a correlation function.

4.3.1 Inversion Method

In the correction vector method proposed by Kühner and White [19] a complex correction vector $|x(z)\rangle$ is defined as

$$|x(z)\rangle = \frac{1}{z - H} A|\psi_0\rangle \ , \tag{4.10}$$

with $z = \omega + i\eta$. Hence the Green's function can be expressed as

$$G_A(z) = \langle\psi_0|A^\dagger|x(z)\rangle \ . \tag{4.11}$$

The correction vector is complex, but one can split it into real and imaginary part to avoid the use of complex numbers

$$|x(z)\rangle = |x^r(z)\rangle + i|x^i(z)\rangle \ . \tag{4.12}$$

Both parts are used as target states. One can find the imaginary part by solving

$$((H - \omega)^2 + \eta^2)|x^i\rangle = -\eta A|\psi_0\rangle \ , \tag{4.13}$$

using an iterative linear system solver like the conjugate gradient (CG) method [21]. This turned out to be difficult for small η and for ω in the vicinity of an eigenvalue of H. It is obvious that the matrix 4.13 becomes singular in this case, the more so as both terms on the left hand side are squared. The problem is getting bad-conditioned.

Knowing the imaginary part, we get the real part directly from:

$$|x^r(z)\rangle = \frac{1}{\eta}(H - \omega)|x^i(z)\rangle \ . \tag{4.14}$$

It turned out to be more efficient, to use the Lanczos procedure in the optimized basis to calculate the spectra, and not to use (4.11) directly [20]. The DMRG basis is optimized to the ground state, the first Lanczos vector $A|\psi_0\rangle$, and the two parts of the correction vector. Two correction vectors can be used to enclose a frequency interval. When the basis converged after a few finite-size sweeps, the Lanczos vector method is applied in the optimized basis resulting in a continued fraction representation of the Green's function.

This way the Green's function is calculated for all ω but it's accurate only in the vicinity of the ω it was optimized for.

We didn't use this trick in our calculations, because we are only interested in testing the performance and accuracy of the method. Instead we used the relation (4.11) to calculate the Green's function.

4.3.2 Projection Method

The new correction approach described below, couldn't produce satisfactory results in the framework of the research for this thesis. The method is nevertheless described in some thoroughness, because it might be promising to implement some modifications, stated below as well.

The basic idea of the correction vector method is based on optimizing the basis to represent a correlation function, concentrating on a specific energy interval. The method described above includes a matrix inversion to gain the imaginary part of the correlation vector (4.13). This problem turned out to be ill conditioned in some cases. It would be desirable to avoid this matrix inversion.

The idea of concentrating on an energy interval can be realized alternatively by using an operator that has finite density of states in the desired energy range and zero density of states anywhere else. If we want to determine a correlation function for the operator A, we can determine an operator that is limited on a frequency interval $[\epsilon_1, \epsilon_2]$ by using a projector. If we denote the energy eigenstates with $|e_i\rangle$ we can construct a projection operator

$$P = \sum_{i \in E} |e_i\rangle\langle e_i| \tag{4.15}$$

with $E = \{i | \langle e_i|H|e_i\rangle \in [\epsilon_1, \epsilon_2]\}$. We project on a subspace of the eigenvectors with eigenvalues in the desired interval.

The operator A is transformed into its energy-sensitive counterpart by a simple multiplication with the projector,

$$A' = PA\ . \tag{4.16}$$

On the energy interval $[\epsilon_1, \epsilon_2]$ the correlation function of A' should look like those of A, but it should vanish anywhere else. A schematic plot can be seen in Fig. 9, where the dotted line symbolizes the density of states for the operator A and the solid line those of A'. Using $A'|\psi_0\rangle$, and perhaps a few Lanczos vectors, as target states, should result in a concentration on the energy interval $[\epsilon_1, \epsilon_2]$.

The problem of matrix inversion in the correction vector method is shifted to the problem of constructing a projection operator on an energy interval in a fast and accurate manner.

To obtain a projector, one has to gain eigenvectors of H with eigenvalues in the desired energy range. One can try to obtain those by a Lanczos procedure. As described in the section on the Lanczos method, we start with the vector

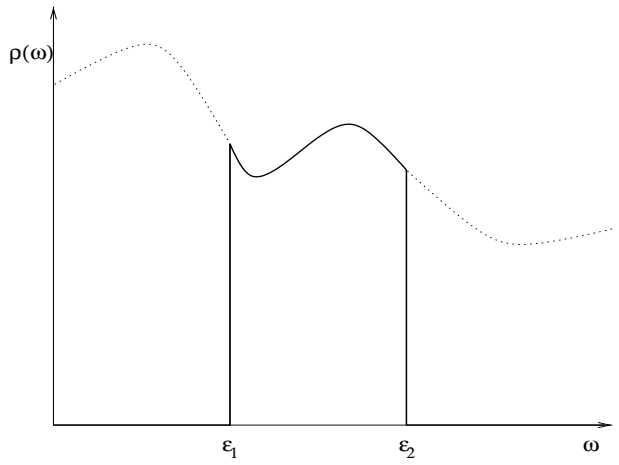

Figure 9: Obtaining a slice of the entire density of states using a projection operator.

$A|\psi_0\rangle$ and span a Krylov space by recursively applying H and orthonormalizing the new vector with respect to the others (4.8). This results in a tridiagonal form of H in the basis of the Lanczos vectors, as seen above. In principle this transformation is exact, if we span a Krylov space of the same dimension as the basis of our system. This is not feasible, of course. Aborting the Lanczos recursion leads to an approximate tridiagonal H, given in a reduced new basis.

The tridiagonal form of H can be readily diagonalized yielding pairs of approximate eigenvalues and corresponding eigenvectors.

This simple method of obtaining eigenvalues and eigenvectors performed not very well, because the approximate eigenvalues are spread over the full eigenvalue range of H, resulting in a very poor resolution in the interval of interest. Even an iterated Lanczos procedure couldn't confine more of the approximate eigenvalues in the interval. An example will be discussed in the following section.

A better density and resolution of eigenvalue-eigenvector pairs in a specified interval might be obtained by numerical method, that is intended to find eigenvectors and eigenvalues in the interior of the spectrum of a matrix. Some of these methods will be stated in the outlook at the end of this thesis.

Provided a good projection operator is given, we can derive the coefficients of a continued fraction expansion of the Green's function by the Lanczos method. $A'|\psi_0\rangle$ and the first few Lanczos vectors are used as target states.

The first few coefficients obtained by applying the Lanczos process on A' reflect the weight of the density of states in the desired interval and the shape

of the curve. As we slice an interval out of the whole density of states function, the terminator of the continued fraction expansion should be chosen accordingly.

To get a good picture of the density of states in an interval, the few coefficients resulting from the Lanczos procedure should be continued in a suitable manner. One should use the coefficients for a box function, i. e. a function that is finite and constant in the interval and vanishes anywhere else. Such a continued fraction expansion can be deduced utilizing the Legendre polynomials. Properly normalized they sum up to a box as described above in the interval $[-1,1]$. The following two formulas are taken from [22]. The Legendre polynomials have a three term recursion relation which reads

$$(n+1)f_{n+1} = (2n+1)xf_n - nf_{n-1} \ . \tag{4.17}$$

The normalization condition reads

$$g_n = f_n\sqrt{\frac{2}{2n+1}} \ . \tag{4.18}$$

This recursion relation corresponds to a continued fraction expansion of the type

$$g_{box}(\omega) = \cfrac{1}{\omega - a_0 - \cfrac{b_0^2}{\omega - a_1 - \cfrac{b_1^2}{\cdots}}} \ . \tag{4.19}$$

The coefficients a_n and b_n resulting in a box function that is nonzero in the interval $[\epsilon_1, \epsilon_2]$, follow from the recursion above and from a transformation on the interval,

$$\begin{aligned} a_n &= \frac{\epsilon_1 + \epsilon_2}{2} \\ b_n &= \frac{\epsilon_2 - \epsilon_1}{2}\frac{n+1}{\sqrt{(2n+2)^2 - 1}} \ . \end{aligned} \tag{4.20}$$

To obtain real and imaginary part, one can terminate the continued fraction at a very high order with a shifted and rescaled version of (2.39), where the interval $[-1,1]$ is mapped on the interval of interest $[\epsilon_1, \epsilon_2]$. The rescaling is done in a manner, that conserves the total weight, i. e. the integral over the interval. The Green's function, with linear real part and half circle shaped imaginary part, transfered on the interval $[\epsilon_1, \epsilon_2]$ reads

$$g_{[\epsilon_1,\epsilon_2]}(\omega) = \left(\frac{2}{\epsilon_2 - \epsilon_1}\right)\left(2\left(\frac{2\omega - \epsilon_1 - \epsilon_2}{\epsilon_2 - \epsilon_1}\right) - 2i\sqrt{\left(\frac{2\omega - \epsilon_1 - \epsilon_2}{\epsilon_2 - \epsilon_1}\right)^2 - 1}\right) \tag{4.21}$$

Continued fraction expansions are usually evaluated in reverse order. We start with the high order terminator, resulting in a rescaled half circle for the imaginary part. Then we use the coefficients (4.20). If we would use this coefficients up to first order, we would obtain a sharp rectangular box. But we discard the coefficients with the lowest indices and insert the coefficients gained from applying the Lanczos process on $A'|\psi_0\rangle$. This should result in a smooth curve inside the interval and a good representation of the square root singularities on the edges of the interval.

4.4 Remarks on the Implementation

The programming language of our choice was C++. The concept of object orientation is quite useful to encapsulate items like matrices, block matrices and blocks of quantum spins. The dynamic use of memory is quite useful to handle the book keeping of stored operators and wave-functions.

The underlying class in our implementation is one for storing matrices and performing simple operations on them. This, as far as possible, is done by calling the fast numeric library routines from LaPack and BLAS. This class has been deduced from a class created by Schönfeld [16].

Furthermore a class for storing and handling block matrices has been implemented. The operators and states in DMRG algorithms are matrices with block structure, where only a small fraction of blocks is densely filled and all the others are zero.

There is a class that stores single site operators and another one that stores blocks, i. e. parts of a spin chain, and all the operators related to them. This class also provides functions to perform basis transformations, append single sites, and so on.

It is a good idea to exploit as many symmetries as possible. The conservation of the total spin leads, a proper sorting of the states assumed, to a blocked structure of operators and wave functions. To store and treat only the nonzero blocks saves a great amount of memory and execution time.

One of the central tasks in the DMRG algorithms is to find the ground state of the superblock Hamiltonian. This is done by by a Davidson-Liu algorithm [23, 24]. In the infinite-size algorithm a stochastic initial guess (stochastic in the subspace with the relevant total spin, of course) is used. During the sweeps in the finite-size algorithm one can reduce the number of Davidson iterations by a factor between 5 and 10 by calculating an initial guess. This is done by transforming

the ground state obtained in the last DMRG step. The transformation of wave vectors via the basis transformation matrices is described in the proceedings [25].

As an iterative eigenproblem solver is used, only products of the superblock Hamiltonian with a wave vector have to be calculated. It is mandatory to calculate these products implicitly, i. e. by using the block operators, and not to store the superblock Hamiltonian. Storing the superblock Hamiltonian would cost so much memory and time that the programs could not be used on normal workstations or the number of basis states is heavily restricted. A Hamiltonian of a superblock, consisting of two blocks and two separate spins, has got a basis of dimension $4 \times m^2$, where m is the dimension of the basis of a block. For $m = 128$ this results in a dimension of $65,536$, for $m = 512$ the dimension of the Hamiltonian is $1,048,576$. Storing one full Hamiltonian for $m = 512$, would mean storing about $1.1 \cdot 10^{12}$ double precision numbers, i. e. 8.8 TeraByte.

The implicit product building results in simple and small matrix block multiplications that can be easily handed to numerical library routines. A good description on how to calculate the superblock Hamiltonian products is given in [25].

The correction vector method includes a linear system solver for problems like $Ax = b$, with real-symmetric matrix A and vectors x and b. The standard methods conjugate gradient (CG) [21] and generalized minimal residuum (GMRES) [26] have been implemented and tested. GMRES is more robust and works even for asymmetric matrices. But for our problem CG converges faster. It turned out, that in the very ill conditioned cases none of the above methods converged satisfactorily.

There are a lot of DMRG specific functions that handle tasks like calculating the density matrix, diagonalizing it, and many more. The logic dissection of all this tasks is not clear without ambiguity, and details of their implementation are omitted here.

5 Results

In the first part of this chapter some DMRG measurements of static properties like the ground state energy for the homogeneous Heisenberg chain and the homogeneous XY-chain are shown. In the framework of these measurements the influence of parameters like chain length and basis size m will be examined.

In the second subsection we discuss DMRG results for the measurement of local dynamic properties. The benchmark will be again a uniform XY-chain, where we examine the local dynamics of the surface spin. Results for the Lanczos method [18] and a correction vector method [19] will be shown.

We will discuss the difficulties with the new correction vector approach which is outlined in section 4.3.2 and make some suggestions that might be suitable to overcome the flaws.

5.1 Static DMRG Results

The Hamiltonian for a uniform isotropic Heisenberg chain reads

$$H_{\text{Heis}} = \sum_n \mathbf{S}_i \mathbf{S}_{i+1} = \sum_n \left(S_i^z S_{i+1}^z + \frac{1}{2} \left(S_i^+ S_{i+1}^- + S_i^- S_{i+1}^+ \right) \right) \quad . \tag{5.1}$$

The exact solution for the ground state energy per site has been derived by Bethe [27]

$$E_{\text{Heis}} = \frac{1}{4} - \ln 2 = -0.4431471 \cdots \quad . \tag{5.2}$$

As stated before in (2.29) the ground state energy per site for an infinite XY-chain is

$$E_{XY} = -\frac{1}{\pi} = -0.3183098 \cdots \quad . \tag{5.3}$$

In Fig. 10 DMRG results for the deviation of the ground state energy per site of a homogeneous XY-chain from the value in the thermodynamic limit (5.3) are shown as a function of $1/L$, where L denotes the number of sites in the chain. The calculations have been done with different numbers of basis states m. The linear behavior of the energy as a function of $1/L$ reflects the conformal invariance of the underlying model. In this plot almost all data points for the different m coincide. Linear extrapolation of the data points in the inset of Fig. 10 yields a very good approximation to the exact limit for basis sizes with 32 sites or more.

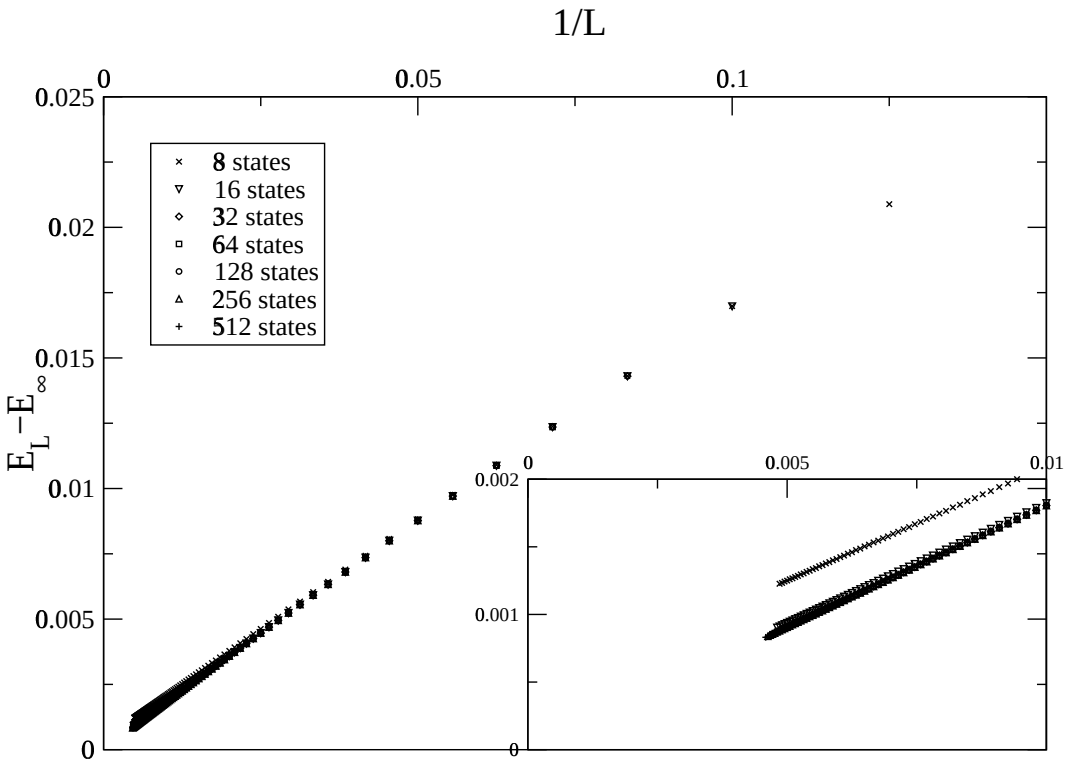

Figure 10: Absolute deviation of ground state energy per site for XY-chains with L sites from the thermodynamic limit calculated for different DMRG basis sizes.

When calculating on very small Hilbert spaces the energy is overestimated due to the poor representation of the system, resulting in an inaccurate ground state vector and hence an inaccurate eigenvalue.

The calculations of the deviation of energy from the limit of an infinite chain for the homogeneous isotropic Heisenberg model (5.1) show exactly the same features, as one can see in Fig. 11.

The plots Fig. 10 and Fig. 11 show that the DMRG algorithm works and the ground state energy values converge towards the thermodynamic limits, provided that the DMRG basis is not to small. But from this plots it is difficult to estimate the dependence of accuracy on the size of the truncated basis and on the size of the treated system.

The exact results (2.28) for the ground state energy of a finite homogeneous XY-chain with L sites, that have been derived in section 2.3, are a better benchmark to test the accuracy of the algorithm. The deviation from zero in Fig. 10

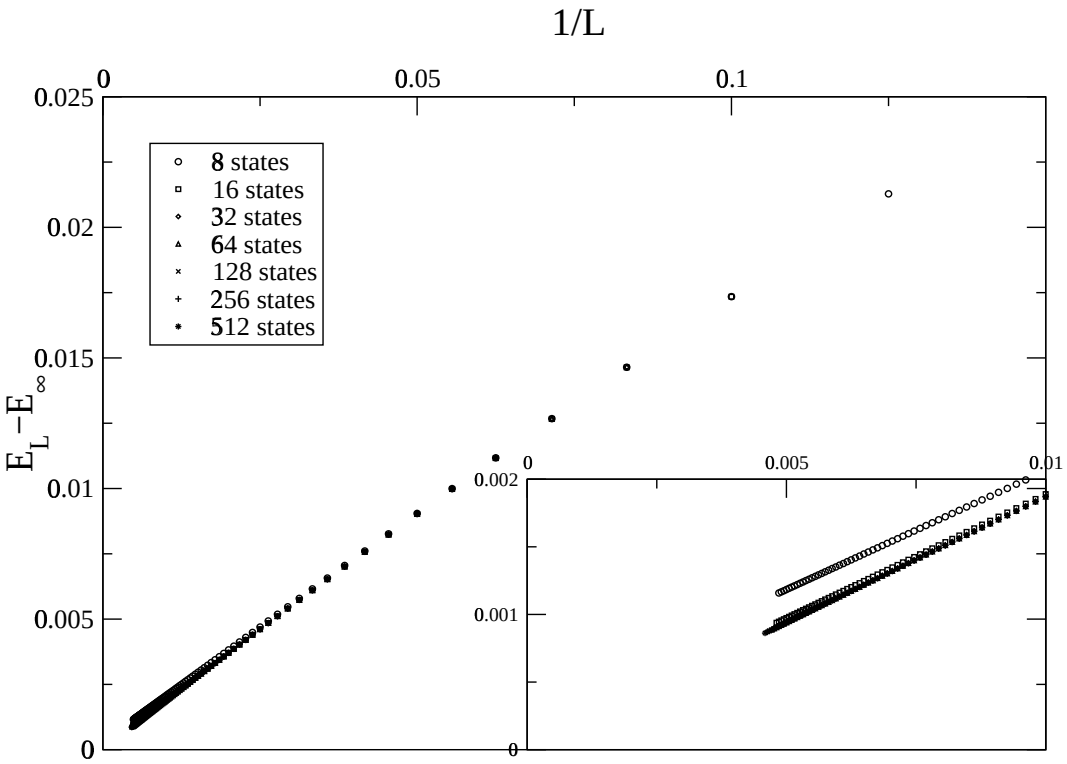

Figure 11: Absolute deviation of ground state energy per site for Heisenberg chains with L sites from the thermodynamic limit calculated for different DMRG basis sizes.

and Fig. 11 is predominantly due to finite size effects. By comparing DMRG results with exact results for finite chains we can isolate the truncation errors.

The development of the relative truncation errors with growing system size is shown for different numbers of basis states m in Fig. 12. This plot reveals some interesting features of DMRG.

For a specific basis size m the error in ground state energy increases rapidly with growing system size for relatively small systems, but the curve flattens for larger systems. This shows that during the first truncations of infinite-size DMRG the relative loss in accuracy is higher than for longer chains. This is due to the fact, that the change in ground state energy per site as a function of growing system size decreases rapidly, as can be seen in Fig. 3. The flattening of the relative error curves seems to show some kind of saturation. The picture that one could have in mind to understand this feature is, that adding a single site to a uniform semi-infinite chain, doesn't change the properties. Hence adding a

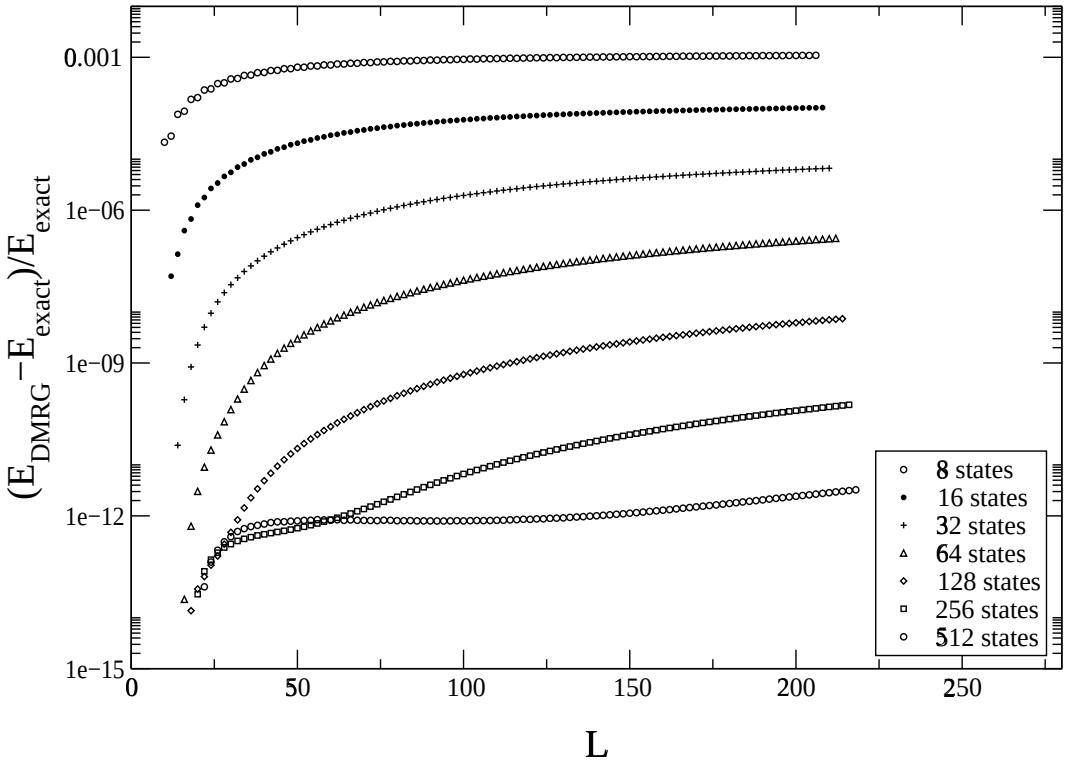

Figure 12: Relative error is the ground state energy of the XY-chain with L sites calculated with DMRG for different basis sizes.

single site to a very long chain that is represented to a certain accuracy should lead to an almost equally good representation of the enhanced chain, even after a basis truncation.

An obvious result of the measurements shown in Fig. 12 is the dependence of the accuracy on the number of states in the truncated basis m. As one would expect the accuracy in ground state energy for a fixed chain length L increases with growing basis size m. Doubling the basis yields an increase in accuracy of one to two orders of magnitude.

Our implementation of the DMRG algorithm allows for calculating systems with 1024 states in the truncated basis on a normal workstation. One could optimize the implementation by adding the single sites on each block implicitly, when calculating the products of the superblock Hamiltonian with a wavevector. This should allow calculations with the doubled number of basis states but with the same storage requirements as in the actual implementation.

It should be considered that doubling the basis leads to a rather significant

increase in runtime. Especially when we are only interested in a good representation of the ground state, i.e. the ground state is the only target state, the accuracy that can be reached with a basis size m of 512 states or 1024 states is very high. Increasing it much further would lead into a region, where numerical round up errors due to limited machine precision become significant. When targeting on a number of states, the accuracy in the representation is splitted among those states. In this case a higher number of states in the basis might be reasonable. But as stated above, runtime and storage requirements limit the arbitrary choice of the basis size m.

In this section DMRG measurements of static properties of spin chains have been presented and they have been compared with the exact results in section 2.3. The DMRG results proved to be in good agreement with the exact results.

5.2 Dynamic DMRG Results

5.2.1 Exact Benchmark Results

Fortunately the XY-chain is simple enough to obtain some exact analytical results for finite and infinite systems. In section 2.3 we have calculated the density of states for infinite XY-chains. For a finite chain the correlation function for the operator S_0^+ is not a continuous function but a set of Dirac delta functions.

Transforming the XY-chain on a chain of spinless fermions via a Jordan-Wigner transformation, as shown in section 2.3, yields an explicit expression for $c_k^\dagger$ (2.24) and the energy eigenvalues (2.26). As we only consider particle creation, that is we have no particle-hole symmetry, we take only the positive eigenvalues into account.

One can explicitly construct a diagonal Hamiltonian matrix containing the positive energy eigenvalues and the operator $c_{k_0}^\dagger$ is given, with $k_0 = \frac{\pi}{L+1}$. The Lanczos procedure described in section 4.2 yields a numerical but exact continued fraction expansion for the Green's function (4.6). The calculation of this continued fraction expansion for the exact Green's functions for finite XY-chains has been done with the computer algebra program `Maple`.

Since the exact Green's function has got poles on the real axis it is difficult to handle it numerically. We don't evaluate it exactly on the real axis but slightly above. This corresponds to the use of $z = \omega + i\eta$ as the argument of the Green's function, where η is a small but finite constant.

The effect of the small η can be understood as a convolution of the Green's function with a Gaussian function of half-width η. In Fig. 13 the imaginary

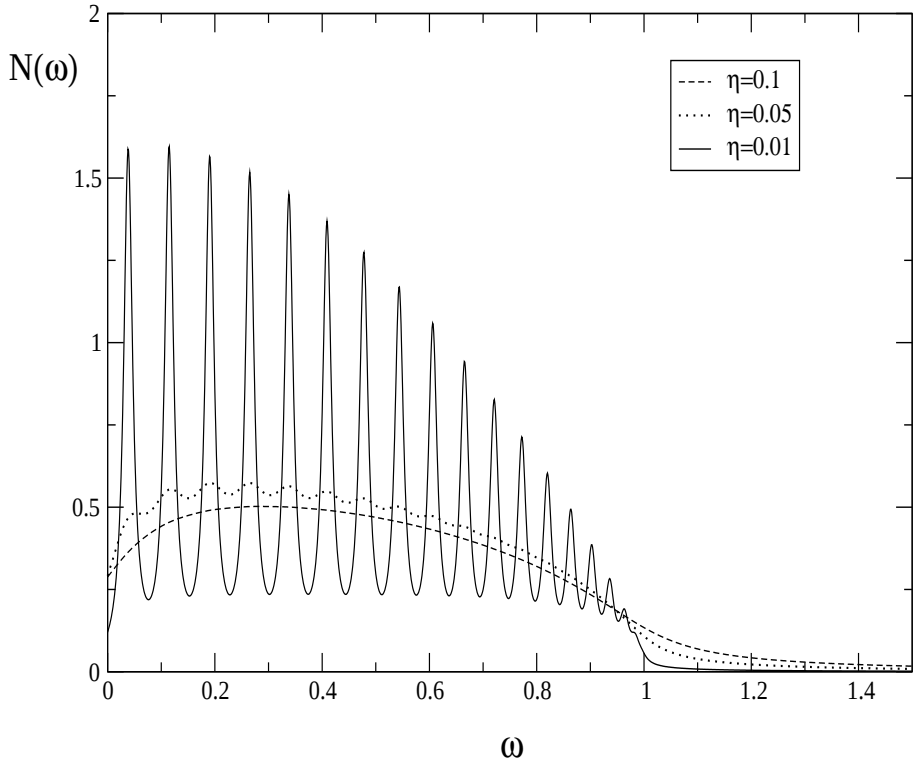

Figure 13: Exact spectral function of a homogenous XY-chain with 40 sites for different broadening factors η.

part of the exact numerical Green's function, rescaled by a factor $-\frac{1}{\pi}$, is plotted for different values of η. This rescaled imaginary part of the Green's function corresponds to the spectral density of states. Although the term "density" only makes sense in the continuum limit, we will use it for finite chains, because our method is intended to yield approximations for the thermodynamic limit, i. e. for infinite or semi-infinite chains.

For $\eta = 0.01$ we get a curve with sharp peaks, corresponding to broadened Dirac delta functions. The peaks are located between zero and one. Their position correspond to the energy eigenvalues of the single particle excitation eigenstates. The tail of the curve for frequencies $\omega > 1$ is caused by the broadening.

Due to the neglect of hole excitations, yielding a neglect of the peaks that correspond to $\omega < 0$, we would expect to see 20 peaks in this half of the spectrum of a 40 site chain. We can't see all of them in Fig. 13. This is due to the broadening, that smears out the low weighted peaks close to $\omega = 1$.

In the curve for $\eta = 0.05$ the sharp peaks disappear. As a rudiment the curve wiggles. The larger broadening factor results in a more distinct tail for $\omega > 1$. The curve for $\eta = 0.1$ is completely smooth and shows no oscillations.

The weight, that is the area below the curves, should be equal for all values of η. This doesn't seem to be true at first sight, because between for $0 < \omega < 1$ the curve for $\eta = 0.1$ lies below the curve for $\eta = 0.05$. This is compensated by the larger tails for $\omega < 0$ and $\omega > 1$ for the curve corresponding to $\eta = 0.1$. The tails below zero aren't shown in Fig. 13.

The exact numerical results for the density of states in Fig. 13 will serve as benchmarks for the accuracy of the DMRG results.

5.2.2 Lanczos Method Results

The Lanczos method, as described in section 4.2, yields the coefficients of the continued fraction expansion of the Green's function. One can directly compare these coefficients with those obtained for the exact Green's function. This is done in Tab. 2 for the Lanczos method results obtained for an XY-chain with 40 sites using 128 basis states and using 4 Lanczos vectors as target states.

The last column of Tab. 2 contains results for an infinite chain. They have been obtained by expanding the positive half of the exact density of states for an infinite chain (2.40) in a series and subsequently transforming the series into a continued fraction. These transformations have been performed with `Maple`. Because of the limited order of the involved series expansion, only the first few rather trustable values are shown.

One can see that the exact values for an infinite and a finite chain differ significantly. It is reasonable to compare the DMRG data with the exact data for finite systems. For the first four a_n and for the first three to four b_n coefficients there is rather good coincidence between the DMRG Lanczos method values and the exact values for a finite chain. From a_4 on the coefficients from the DMRG results differ significantly from the exact data. As we used four Lanczos vectors as target states this is not very surprising. Only the first four vectors in the Lanczos process are accurately represented by the basis, yielding the same coefficients as in the exact case.

If one just examines the continued fraction expansion coefficients it is hard to judge how much information is lost due to the DMRG truncation. To produce curves that are comparable to the curves in Fig. 13 we evaluated the continued fractions defined by the coefficients from the Lanczos method DMRG results.

Table 2: Coefficients in continued fraction expansion of the Green's function. Values calculated with DMRG Lancos method for a 40 site XY-chain, numerical results for an exactly treated 40 site chain and an infinite chain. The latter both were obtained via Maple.

coefficient	40 sites Lanczos	40 sites exact	infinite chain
a_0	0.424725738265	0.424725035993	0.424413181578
b_0^2	0.069606556827	0.069608643801	0.0698734513025
a_1	0.488739886307	0.488720315499	0.486690764913
b_1^2	0.0634846105569	0.063494585957	0.0643638064851
a_2	0.500587005893	0.500509903823	0.495293124973
b_2^2	0.0614363144237	0.061474718068	0.0633196956714
a_3	0.507857538937	0.507533240397	0.497591805251
b_3^2	0.0595993477044	0.059767760911	0.0629635192219
a_4	0.517439881421	0.514796068471	0.498532204741
b_4^2	0.0779777022036	0.057873952346	0.0627986190925
a_5	5.68251125659	0.523274771933	0.498999473066
b_5^2	73.0826526131	0.055673011692983	0.0590199656762
a_6	14.8409723162	0.5333325289555	⋮
b_6^2	2.70118341671	0.053121971602	
a_7	16.8010960412	0.54519742344	
b_7^2	25.3760793042	0.050201947372	
⋮	⋮	⋮	

Again the continued fractions have been evaluated for $z = \omega + i\eta$, introducing the small broadening factor η. The Lanczos method DMRG results for the spectral density for different values of η are shown in Fig. 14. One can see at once, that the DMRG results show the expected rapid decay for $\omega > 1$ and the area below the curves is comparable for the different η and of the same order of magnitude as in the exact case in Fig. 13.

Although only a few Lanczos vectors have been used as target states, we used more than just the few coefficients that correspond to the Lanczos vectors that

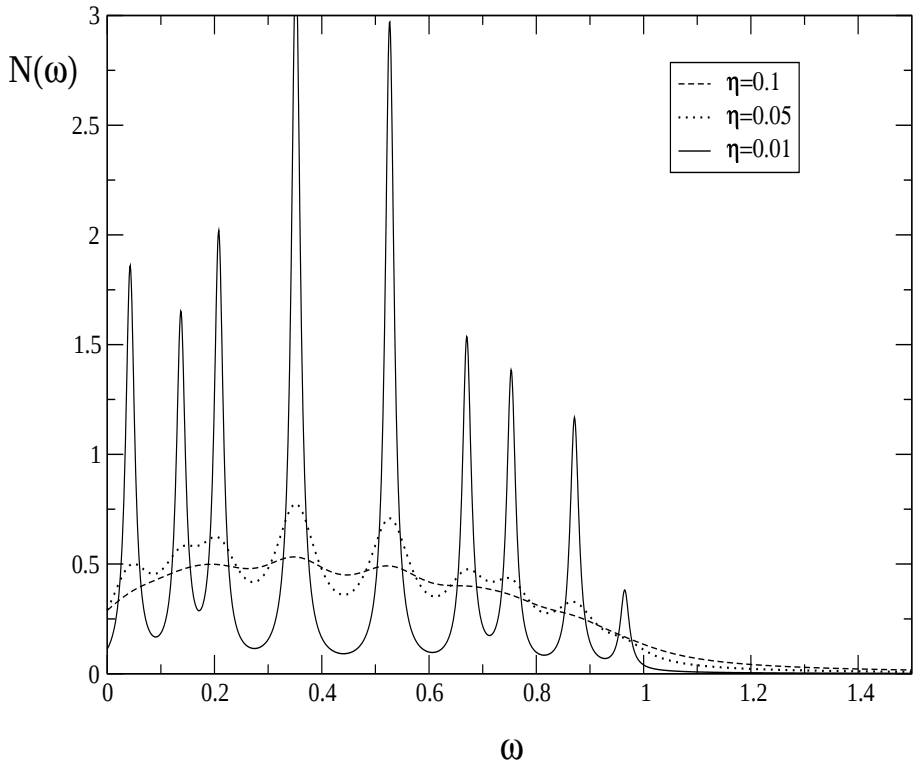

Figure 14: Lanczos DMRG results for the spectral function of a homogenous XY-chain with 40 sites for different broadening factors η.

have been target states. We used the number of coefficients that corresponds to the number of peaks that we expect to see, i. e. in our case half the number of sites in the chain. The coefficients of higher order differ significantly from those of the exact expansion, but they seem to contain some information about the system. Using only the coefficients corresponding to the vectors that have been target states, would result in four peaks in the approximate spectral function. Using more coefficients leads to additional peaks, as can be seen in Fig. 14. For bigger values of the broadening factor η the additional peaks yield smoother curves that are closer to the exact ones.

For a comparison of the Lanczos method DMRG results with the exact spectral functions for the 40 site XY-chain see Fig. 15. In the curves for $\eta = 0.01$ one can resolve the number and the positions of the peaks. Only the first peak in the DMRG curve coincides with a peek of the exact spectrum. Nevertheless the distribution of the weight seems to be correctly represented, as one can see in the curves for larger η.

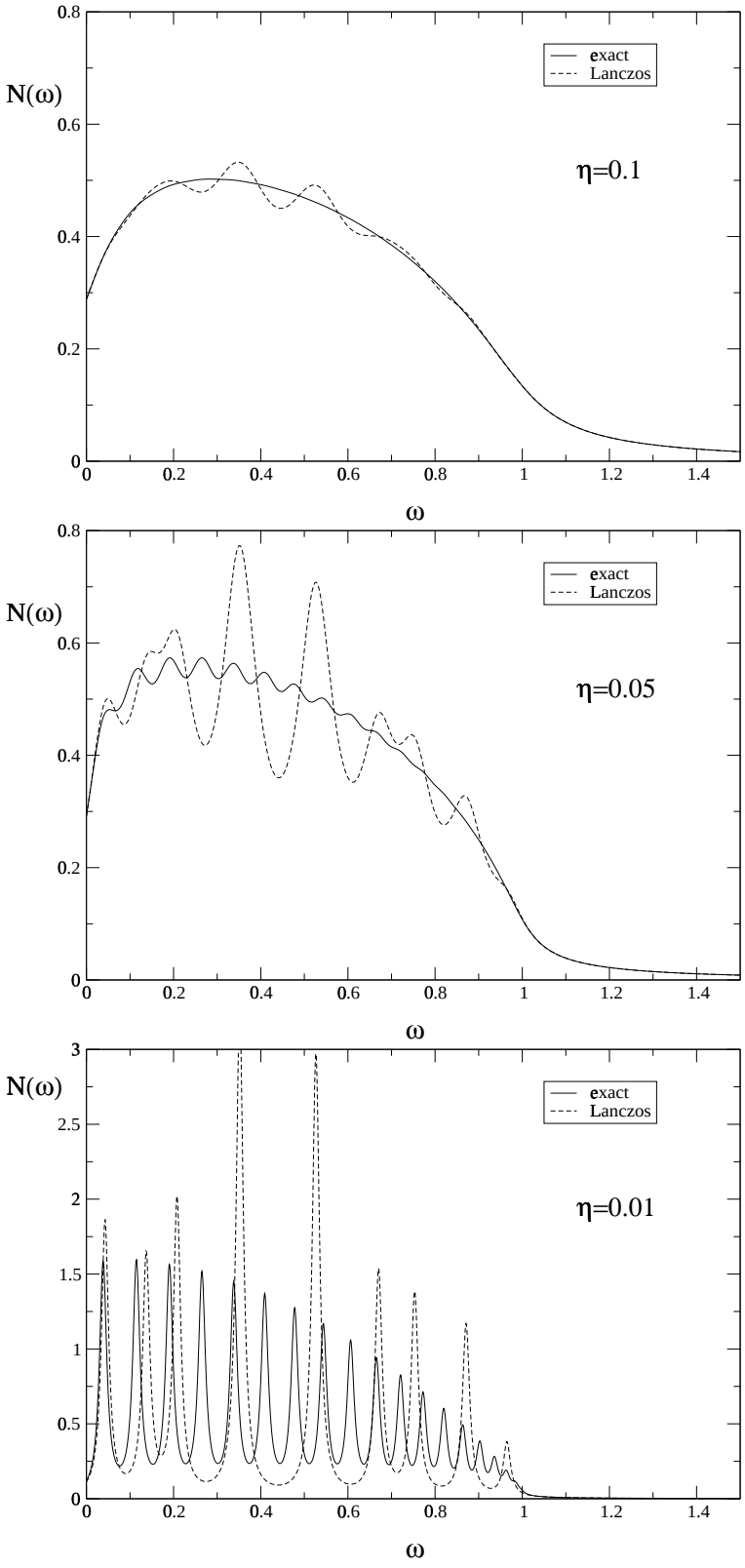

Figure 15: Lancos method DMRG results for the spectral functions of a 40 site XY-chain with 128 basis states and 4 Lanczos vectors used as target states compared to the exact spectral functions for $\eta = 0.1, 0.05, 0.01$.

The exact curves and the DMRG curves coincide as ω approaches zero or one. In between the Lanczos curves oscillate around the exact curves. For $\eta = 0.1$ the deviations become small and the DMRG data give a good picture of the distribution of spectral weight.

The limitations in accuracy are predominantly due principle flaws of the method. The data we obtain for a basis of 256 states while using 8 Lanczos vectors as target states are shown in Fig. 16. The amplitudes of the oscillations around the exact curves for $\eta = 0.1$ and $\eta = 0.05$ are slightly smaller than in Fig. 15. The first three peaks in the DMRG data in Fig. 16 for $\eta = 0.01$ almost coincide with those for the exact spectral function. The total number of peaks in the Lanczos curve has not changed significantly. The data in Fig. 15 and Fig. 16 show very similar deviations between Lanczos method DMRG data and the exact data.

One can conclude, that this is due to the small number of correctly represented peaks. The small number of peaks is enough to show the rough overall distribution of spectral weight, but even for large broadening the spectral weight functions oscillate around the exact broadened curves.

One might think of this dilute distribution of peaks in the approximate spectral function as an effect due to the relative small system size, yielding relatively few peaks in the exact spectral function. The exact spectral functions for an XY-chain with 100 sites and the spectral functions, obtained by the Lanczos method with 128 basis states and using 4 Lanczos vectors as target states, are shown in Fig. 17.

The exact curve for $\eta = 0.01$ shows a large number of peaks. Without any broadening the curve would contain exactly 50 Dirac delta functions. The large number of peaks yields a smooth curve for the larger broadening factors $\eta = 0.05$ and $\eta = 0.01$.

The spectral function obtained via the Lanczos method shows just a few dominant peaks for $\eta = 0.01$. The curves for $\eta = 0.05$ and $\eta = 0.1$ oscillate around the exact curves. The oscillations have similar magnitude and shape as for the 40 site chain in Fig. 15. Hence the resolution of Lanczos method doesn't seem to improve for longer chains.

One can conclude that the Lanczos method has proved to be suitable for the calculation of the spectral functions. The exact position and number of peaks cannot be determined, but the rough distribution of spectral weight is correctly represented. The representation is accurate for larger broadening factors η if ω is close to zero. The decay as ω approaches one is correctly described, too. In

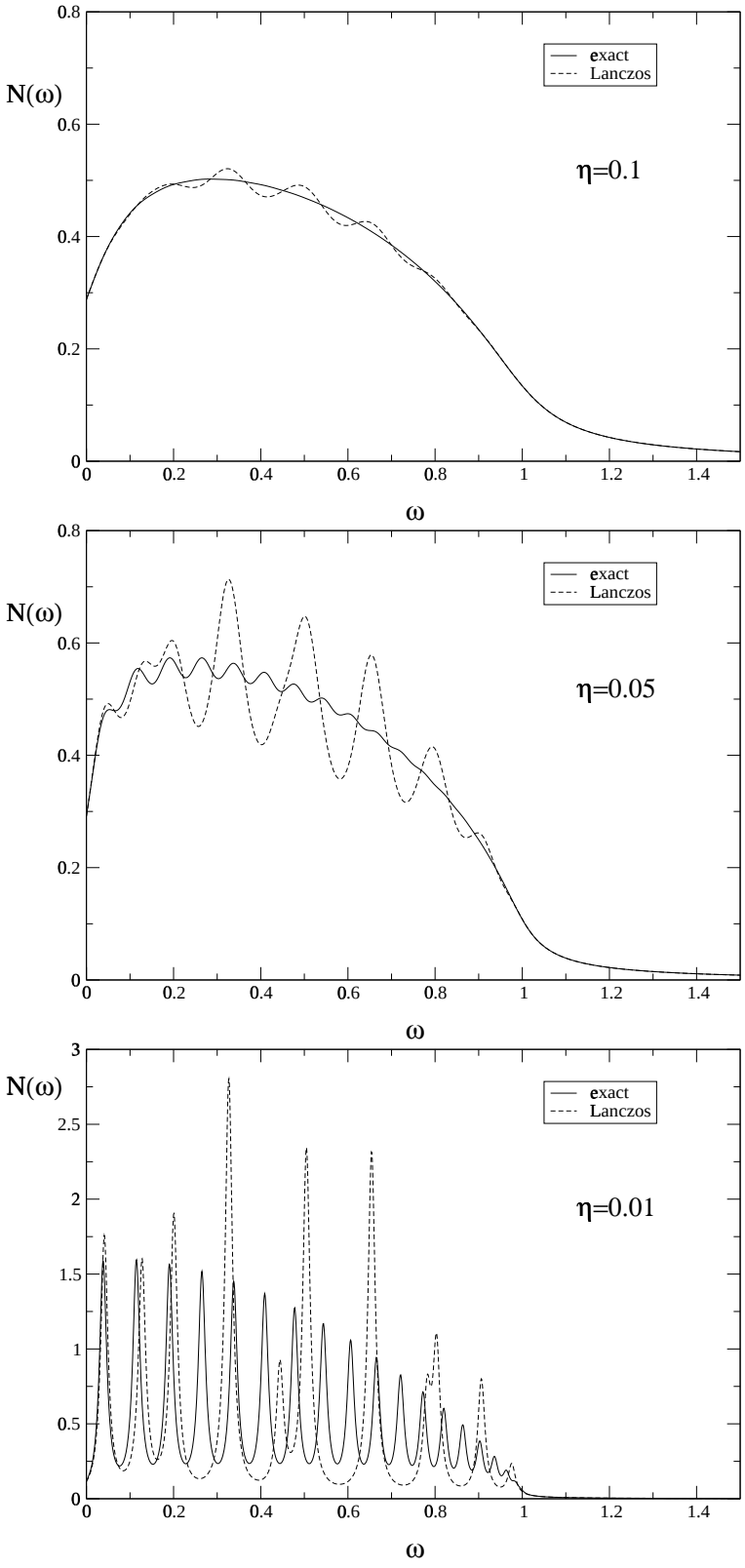

Figure 16: Lancos method DMRG results for the spectral functions of a 40 site XY-chain with 256 basis states and 8 Lanczos vectors used as target states compared to the exact spectral functions for $\eta = 0.1, 0.05, 0.01$.

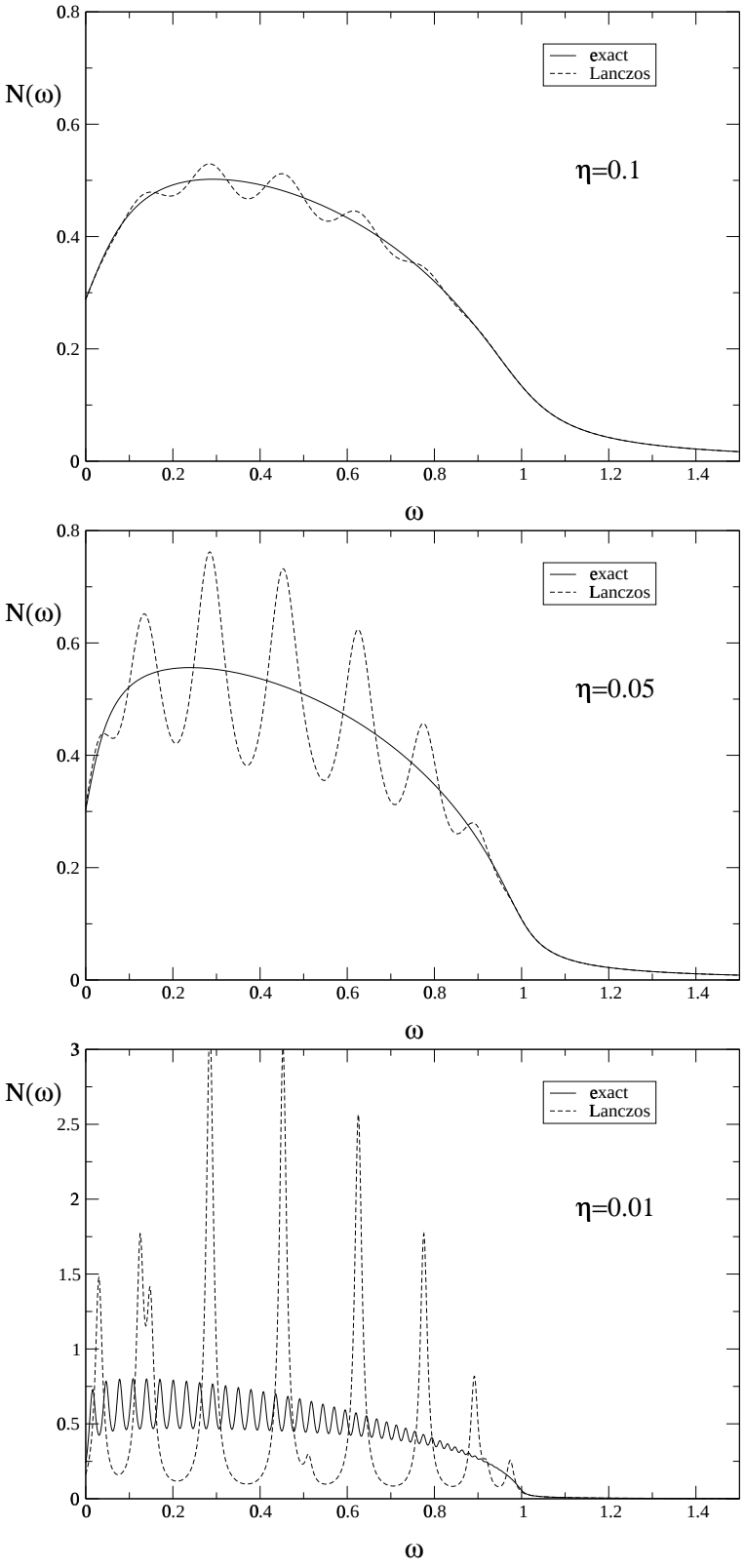

Figure 17: Lancos method DMRG results for the spectral functions of a 100 site XY-chain with 128 basis states and 4 Lanczos vectors used as target states compared to the exact spectral functions for $\eta = 0.1, 0.05, 0.01$.

between the spectral weight is distributed among only a few number of peaks. This yields a good representation of the rough shape of the exact curve but the approximate curve shows coarse, oscillating deviations from the exact data. For small broadening factors η and short chains with distinguishable peaks in the exact curve, only the lowest lying peaks can be represented approximately.

5.2.3 Correction Vector Inversion Method Results

The correction vector method due to Kühner and White has been described in section 4.3.1.

For the homogenous XY-chains and for a broadening parameter $\eta = 0.01$ the matrix inversion (4.13) needed as many as 300 up to 4000 steps of the iterative conjugate gradient method. This corresponds to 600 up to 8000 Hamiltonian matrix vector products.

The time needed to find the ground state of the Hamiltonian turned out to be almost negligible compared to the enormous consumption of runtime due to the matrix inversions.

Apart from these runtime problems the basis and hence the correction vector failed to converge for small values of η. The values for the spectral function jump from finite size sweep to finite size sweep. For low energies ω convergence could be achieved even for small values of η.

Some of the data obtained via the correction vector method are shown in Fig. 18. The plots show correction vector method DMRG data for an XY-chain with 40 sites using 128 basis states and different broadening factors η. We targeted on one correction vector and assigned 40% of the weight to the ground state 30% to the vector $S_0^+|\psi_0\rangle$ and 30% on the imaginary part of the correction vector. The broadened exact curves have been plotted for comparison.

The DMRG data points have been calculated by multiplication of the ground state wavevector and the imaginary part of the correction vector (4.11). Five DMRG sweeps have been performed for each value of ω and the values for the latter three have been plotted. Hence one can figure out where the basis failed to converge.

In the plot for $\eta = 0.1$ all data points coincide, i.e. the basis converged for all values of ω. For values of ω below about 0.2 and above about 0.8 the DMRG data match the exact curve. In between small deviations apear. Interpolating the data would lead to a curve that is similar the curves obtained by the Lanczos method.

The plot for $\eta = 0.05$ confirms the high accuracy for low energies. For $\omega > 0.2$ the data points show deviations from the exact curves. The deviations are oscillating but the magnitude is smaller than for the Lanczos data in Fig. 15. For ω values between about 0.4 and 0.9 the basis fails to converge. This remains true if we perform 10 or 20 sweeps instead of just five sweeps. The high energy data, i. e. in our case ω approaches the value one, are coincident with the exact values.

The high accuracy in the correctly represented low energy region is confirmed by the data for $\eta = 0.01$. The first four peeks of the exact spectrum are represented very well by the correction vector data. For higher energies the basis fails to converge. Solely the decay to zero for ω values in the vicinity of one is represented correctly.

The lacking convergence in the basis and the bad conditioning of the matrix inversion problem (4.13) show up in the same range of the parameter omega. The problem appears for longer chains as well as for a larger basis. It proved not to be a problem of the weight assigned to the correction vector as target state. Targeting on real and imaginary part of the correction vector or using only the imaginary part, didn't change the overall problem.

We tried various modifications of the CG method [21] for matrix inversion. For example we experimented with the explicit restart of the method to add some numerical stability by "reminding" the algorithm of the right hand side of 4.13. We also implemented the GMRES method [26]. We also implemented a deflated version of CG [28], where deflation means the implicit removal of a small number of eigenvectors, i. e. eigenvectors to the left hand side of (4.13), with eigenvalues that are very close to the origin. This method is numerically equivalent to preconditioning methods. Up to now we avoided to use explicit preconditioning methods, because construction, storage and application of a preconditioning matrix is complicated by the fact, that the inversion matrix is very large and not explicitly given. Neither the convergence rate for the matrix inversion nor the convergence of the basis could be improved.

The correction vector inversion method proved to be highly accurate in the determination of spectral functions for energies in the vicinity of the ground state energy. A reason for this might be, that the ground state and hence properties as low energies are well described, due to the choice of the ground state as predominant target state.

For larger energies the method only yielded stable results for large broadening factors η in the order of 0.1. As the data in this energy range are not as accurate

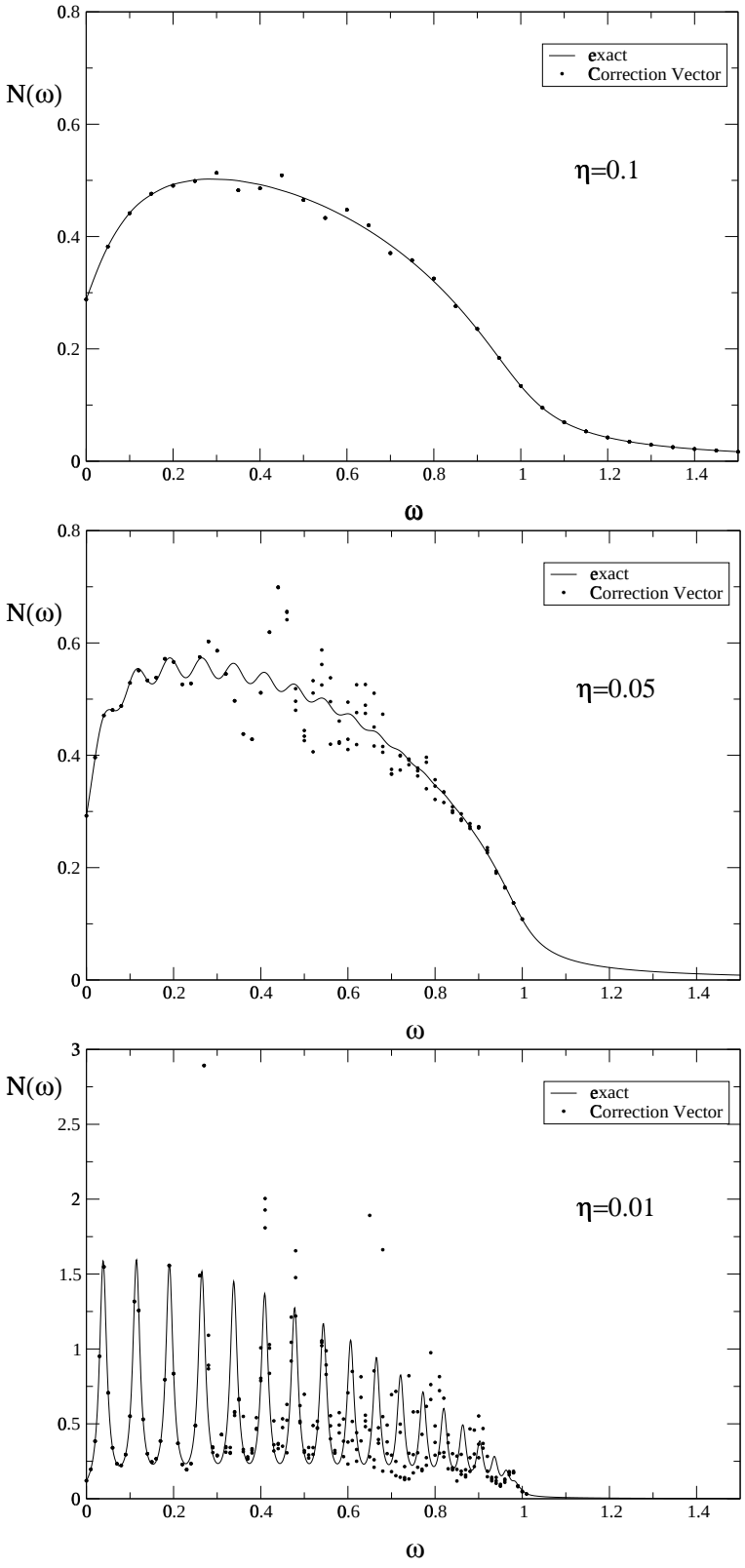

Figure 18: Correction vector method DMRG results for the spectral functions of a 40 site XY-chain with 128 basis states compared to the exact spectral functions for $\eta = 0.1, 0.05, 0.01$.

as in the low energy range, it is probably preferable to use the Lanczos method with a larger basis instead of the correction vector inversion method. This should result in shorter runtimes of the programs, due to the avoidance of the matrix inversions.

The measurements above have been made by using one correction vector as target state and obtaining the data from multiplying ground state and correction vector (4.11). In references [20] and [19] it is suggested to use two correction vectors and to use the Lanczos method on the converged system to obtain the data for the interval. One could try if for the critical range of ω the Lanczos procedure yields reasonable data, despite the fact that the basis is correction vector is not converged.

Further research can be suggested in the field of improving the condition of the linear problem (4.13), perhaps by means of explicit preconditioning.

5.2.4 Correction Vector Projection Method Results

The problems with the correction vector inversion method described in the foregoing section led to the idea of the new correction vector projection method, described in section 4.3.2.

No data have been obtained because we didn't yet manage to construct a projection operator. The aim is to project on a specific energy interval. This problem is equivalent to finding a set of approximate eigenvectors with eigenvalues in the desired range.

We experimented with spanning a Krylov space using the Lanczos procedure and diagonalizing the resulting tridiagonal matrix. This yields a set of approximate eigenvalues with corresponding eigenvectors. Similar to the observations in the section 5.2.2 when discussing the dilute distribution of peaks in the spectra measured via the Lanczos method, only a small fraction of the obtained approximate eigenvalues are located in the desired range.

Starting with the vector $S_0^+|\psi_0\rangle$, the Lanczos procedure, basically consisting of the iterated application of the Hamiltonian followed by orthogonalization and normalization, should yield a set of vectors that is confined in the subspace which is connected to the ground state by a single spin excitation respectively a single particle creation in the fermionic picture. This would result in a confinement of the energy eigenvalues to the interval $0 \leq \omega \leq 1$. The iterated basis truncations and transformations yield a mixing of the states, resulting in the removal of the restriction on the subspace. The approximate eigenvalues distribute over the full

eigenvalue range of the Hamiltonian.

The attempt to construct a projection operator for the energy interval $0 \leq \omega \leq 1$ failed due to the fact that even for 200 Lanczos vectors only two or sometimes three approximate eigenvalues fell in the interval.

Using the projected operator of the approximate eigenvectors as target states didn't result in a higher number of eigenvalues inside the interval. Iterating the Lanczos procedure several times, i. e. starting a new Lanczos procedure with the projected operator, didn't yield a more dense distribution of eigenvalues inside the interval of interest.

One can conclude that the Lanczos procedure is unable to produce a dense distribution of approximate eigenvalues and corresponding eigenvectors in specific frequency interval. This result is in agreement with the the dilute distribution of peaks in the spectra obtained by the application of the the Lanczos method in section 5.2.2.

To continue the research in this field one could use a method that is capable of the direct calculation of interior eigenvalues and corresponding eigenvectors.

The eigenproblem solver due to Davidson and Liu [23], which we use to find the ground state of the Hamiltonian, is only capable of the determination of a set of extreme eigenvectors.

In reference [29] a modification of the Davidson algorithm is proposed that may be useful for the computations of nonextremal eigenvalues.

Another method, proposed in reference [30], to calculate interior eigenvalues of physical systems is based on the minimum residual method.

6 Conclusion

In this thesis the local dynamics of the homogeneous XY-chain have been examined numerically. The XY-chain served as benchmarking system for the accuracy of the DMRG methods. The spectral functions could be measured and the comparison with exact numerical data revealed the abilities and the flaws of different numerical approaches.

This thesis is a preparatory work for the accurate determination of local propagators for single impurity models. The exact determination of these properties is important to make the methods applicable in a local impurity self consistent approach to strongly correlated fermion systems. The mapping of lattice models of strongly correlated fermions onto effective single impurity models in the framework of dynamical mean field theory (DMFT) is exact in the limit of infinite coordination number [4]. The full information on fluctuations in time is kept [5–7] and one gains a self consistent approach [8, 9] to determine the dynamics of fermion lattice models.

In chapter 2 the Anderson model and the Kondo model of single impurities are described. The mapping of the models onto a linear chain is outlined followed by a description of the mapping onto a spin chain via the Jordan-Wigner transformation [10]. The homogeneous XY-chain is introduced and the mapping on a chain of spinless fermions is used to derive static and dynamic properties of finite and infinite XY-chains.

In chapter 3 the density-matrix renormalization group due to White [12, 15] is introduced. The foundations of the density-matrix renormalization are outlined and the algorithmic realizations in form of the infinite-size algorithm and the finite-size algorithm are presented. Finally it is explained how to obtain expectation values, which is a simple task for local single particle operators.

The application of DMRG to gain information on dynamic properties is reviewed in chapter 4. Dynamical correlation functions and their connection to Green's functions are introduced. A description of the Lanczos method suggested by Hallberg [18], that optimizes the DMRG basis for the ground state and a set of Lanczos vectors, is given. Subsequently the correction vector method due to Kühner [19, 20] is outlined. To avoid ambiguities this method is denoted as correction vector inversion method, due to the involved matrix inversion. A description of a correction vector projection approach is given. This method has not yet been implemented successfully. It is based on the construction of a projection operator which is selective in energy. The chapter ends with remarks on

the implementation of the algorithms.

The results are shown in chapter 5. The measurements of the static properties with DMRG methods are included. The correct value of the ground state energy of the Heisenberg chain and of the XY-chain could be reproduced as the limit in the infinite-size DMRG algorithm. The exact values for the ground state energy of finite XY-chains are used to determine the relative error in the ground state energy of the DMRG data for different sizes of the DMRG basis. The gain in accuracy by the increase of basis size is discussed. The measurements of the static properties proved that the implementation of the DMRG algorithm works and gave an impression of the accuracy and its dependence on parameters like basis size and chain length.

Exact numerical data for the local dynamical correlation functions for finite XY-chain are presented and discussed. A description of how the data have been obtained is given. These data served as benchmarks for the following DMRG results.

The results obtained by the Lanczos method are shown. The spectral functions for different broadenings are displayed and compared with the exact data. The influence of larger basis size and the use of more Lanczos vectors as target states on the measurements are discussed. The Lanczos method succeeded in reflecting the correct overall distribution of spectral weight but is only accurate for low energies and it succeeds in correctly representing the rapid decay for high energies. For medium energies the Lanczos data oscillate around the exact curve. This is due to the low number of peaks in the obtained correlation function. This flaw in the representation is a fundamental problem of the Lanczos method, because it couldn't be substantially improved by examining larger systems or by using larger basis sizes and taking more Lanczos vectors as basis states.

The measurements with the correction vector inversion method yielded an excellent reproduction of the exact spectral functions for low energies. For higher energies the involved inversion problem becomes increasingly ill-conditioned. Furthermore the correction vectors in the higher energy range fail to converge during the DMRG sweeps. The rapid decay for $\omega > 1$ is represented correctly. We propose to try to gain a better condition for the inversion matrix by some kind of preconditioned method.

As the correction vector method due to Kühner failed to produce reliable data in the whole interval of interest, a different correction vector approach is proposed. This approach has not yet been developed to operativeness, and can be understood as a suggestion for further research. As the method strongly

depends on the construction of a projection operator, which is selective in energy, we proposed some methods to obtain approximate eigenvalues and corresponding eigenvectors in a given range [29, 30].

This thesis is intended as starting point for the research that should lead to an iterative local impurity self consistent algorithm for strongly correlated fermion lattices in the limit of infinite coordination number. A DMRG algorithm is intended to yield the local propagators at the impurity site, which are subject to the self consistency condition.

References

[1] J. Kondo, Prog. Theor. Phys. **32**, 37 (1964).

[2] P. W. Anderson, Phys. Rev. **124**, 41 (1961).

[3] A. C. Hewson, *The Kondo Problem to Heavy Fermions* (Cambridge University Press, Cambridge, 1993).

[4] W. Metzner and D. Vollhardt, Phys. Rev. Lett. **62**, 324 (1989).

[5] E. Müller-Hartmann, Z. Phys. B **74**, 507 (1989).

[6] M. Jarrell, Phys. Rev. Lett. **69**, 168 (1992).

[7] A. Georges and G. Kotliar, Phys. Rev. B **45**, 6479 (1992).

[8] T. Pruschke, M. Jarrell, and J. K. Freericks, Adv. Phys. **44**, 187 (1995).

[9] A. Georges, G. Kotliar, W. Krauth, and M. J. Rozenberg, Rev. Mod. Phys. **68**, 13 (1996).

[10] P. Jordan and E. Wigner, Z. Phys. **47**, 631 (1928).

[11] K. G. Wilson, Rev. Mod. Phys. **47**, 773 (1975).

[12] S. R. White, Phys. Rev. Lett. **69**, 2863 (1992).

[13] K. Hallberg, cond-mat/9910082 (1999).

[14] J. R. Schrieffer and P. A. Wolff, Phys. Rev. **149**, 491 (1966).

[15] S. R. White, Phys. Rev. B **48**, 10345 (1993).

[16] F. Schönfeld, Ph.D. thesis, Universität zu Köln, 1999.

[17] G. H. Golub and C. F. van Loan, *Matrix computations* (John Hopkins University Press, Baltimore and London, 1996).

[18] K. Hallberg, Phys. Rev. B **52**, 9827 (1995).

[19] T. D. Kühner and S. R. White, Phys. Rev. B **60**, 335 (1999).

[20] T. D. Kühner, Ph.D. thesis, Universität Bonn, 1999.

[21] M. R. Hestenes and E.Stiefel, J. Res. Nat. Bur. Stand. **49**, 409 (1952).

[22] M. Abramowitz and I. A. Stegun, *Handbook of Mathematical Functions* (Dover Publisher, New York, 1964).

[23] E. R. Davidson, Computers in Physics **7**, 519 (1993).

[24] E. R. Davidson, J. Comput. Phys. **17**, 87 (1975).

[25] I. Peschel, X. Wang, M. Kaulke, and K. Hallberg, *Density-Matrix Renormalisation* (Springer, Berlin, 1999).

[26] Y. Saad and M. H. Schultz, SIAM J. Sci. Stat. Comput. **7**, 856 (1995).

[27] H. Bethe, Z. Phys. **71**, 205 (1931).

[28] Y. Saad, M.Yeung, J. Erhel, and F. Guyomarc'h, SIAM J. Sci. Comput. **21**, 1909 (2000).

[29] G. L. Sleijpen and H. A. van der Horst, SIAM J. Matrix Anal. Appl. **17**, 401 (1996).

[30] H.-G. Yu and N. G, J. Chem. Phys. **110**, 11133 (1999).

Danksagung

Ich möchte mich an dieser Stelle sehr herzlich für die gute Betreuung durch Priv.-Doz. Dr. Götz S. Uhrig bedanken.

Mein Dank gilt auch besonders Prof. Dr. Hartmut Monien für die Betreuung dieser Arbeit in der Rolle des Koreferenten.

Ich bedanke mich bei Prof. Dr. Erwin Müller-Hartmann, dem Leiter meiner Arbeitsgruppe in Köln.

Dr. F. Schönfeld und T. D. Kühner danke ich für die interessanten Diskussionen über die Dichtematrixrenormierung.

Für die nette Arbeitsatmosphäre und die Unterstützung bei der Durchsicht der Arbeit danke ich Carsten Raas, Boris Marić und Robert Schmitz.